Mon. Not. R. Astron. Soc. **000**, 000–000 (0000) Printed 12 June 2002 (MN LATEX style file v2.2)

Relativistic models and the jet velocity field in the radio galaxy 3C 31

R.A. Laing ⋆[1,2], A.H. Bridle[3]
[1] *Space Science and Technology Department, CLRC, Rutherford Appleton Laboratory, Chilton, Didcot, Oxon OX11 0QX*
[2] *University of Oxford, Department of Astrophysics, Denys Wilkinson Building, Keble Road, Oxford OX1 3RH*
[3] *National Radio Astronomy Observatory, 520 Edgemont Road, Charlottesville, VA 22903-2475, U.S.A.*

Received

ABSTRACT

We compare deep VLA imaging of the total intensity and linear polarization of the inner jets in the nearby, low-luminosity radio galaxy 3C 31 with models of the jets as intrinsically symmetrical, decelerating relativistic flows. We show that the principal differences in appearance of the main and counter-jets within 30 arcsec of the nucleus can result entirely from the effects of relativistic aberration in two symmetrical, antiparallel, axisymmetric, time-stationary relativistic flows. We develop empirical parameterized models of the jet geometry and the three-dimensional distributions of the velocity, emissivity and magnetic-field structure. We calculate the synchrotron emission by integration through the models, accounting rigorously for relativistic effects and the anisotropy of emission in the rest frame. The model parameters are optimized by fitting to our 8.4-GHz VLA observations at resolutions of 0.25 and 0.75 arcsec FWHM, and the final quality of the fit is extremely good. The novel features of our analysis are that we model the two-dimensional brightness distributions at large number of independent data points rather than using one-dimensional profiles, we allow transverse as well as longitudinal variations of velocity, field and emissivity and we simultaneously fit total intensity and linear polarization.

We conclude that the jets are at $\approx 52^\circ$ to the line of sight, that they decelerate and that they have transverse velocity gradients. Their magnetic field configuration has primarily toroidal and longitudinal components. The jets may be divided into three distinct parts, based not only on the geometry of their outer isophotes, but also on their kinematics and emissivity distributions: a well-collimated inner region; a flaring region of rapid expansion followed by recollimation and a conical outer region. The inner region is poorly resolved, but is best modelled as the sum of fast ($0.8 - 0.9c$) and much slower components. The transition between inner and flaring regions marks a discontinuity in the flow where the emissivity increases suddenly. The on-axis velocity stays fairly constant at $\approx 0.8c$ until the end of the flaring region, where it drops abruptly to $\approx 0.55c$, thereafter falling more slowly to $\approx 0.25c$ at the end of the modelled region. Throughout the flaring and outer regions, the velocity at the edge of the jet is ≈ 0.7 of its on-axis value. The magnetic field in the flaring region is complex, with an essentially isotropic structure at the edge of the jet, but a more ordered toroidal+longitudinal configuration on-axis. In the outer region, the radial field vanishes and the toroidal component becomes dominant. We show that the emissivity and field structures are inconsistent with simple adiabatic models in the inner and flaring regions. We suggest that the discontinuity between the inner and flaring regions could be associated with a stationary shock structure and that the inferred transverse velocity profiles and field structure in the flaring region support the idea that the jets decelerate by entraining the external medium. We demonstrate the appearance of our model at other angles to the line of sight and argue that other low-luminosity radio galaxies resemble 3C 31 seen at different orientations.

Key words: galaxies: jets – radio continuum:galaxies – magnetic fields – polarization – MHD

E-mail: R.A.Laing@rl.ac.uk

1 INTRODUCTION

The flow parameters of jets in extragalactic radio sources have hitherto proven difficult to determine because of the absence of unambiguous diagnostics. Most progress has been made in the estimation of velocities, particularly where these are thought to be relativistic. The idea that jets in low-luminosity, i.e. FR I (Fanaroff & Riley 1974), radio galaxies have relativistic speeds rests on five main arguments:

(i) evidence for relativistic motion on parsec scales in BL Lac objects, coupled with the hypothesis that they are FR I radio galaxies observed at small angles to the line of sight (Urry & Padovani 1995);
(ii) measurement of apparent proper motions with speeds up to at least c in M 87 (Biretta, Zhou & Owen 1995);
(iii) modelling of relativistic flows, which demonstrates the feasibility of deceleration on kiloparsec scales in realistic galactic atmospheres (Bicknell 1994; Komissarov 1994; Bowman, Leahy & Komissarov 1996);
(iv) the interpretation of correlated depolarization asymmetry and jet sidedness in FR I sources (Morganti et al. 1997) as a consequence of Doppler beaming and foreground Faraday rotation (Laing 1988);
(v) observations of brightness and width asymmetries in FR I jets which decrease with distance from the nucleus and are correlated with fractional core flux, implying that they decelerate and are faster on-axis than at their edges (Laing 1993, 1996; Hardcastle et al. 1997; Laing et al. 1999).

This paper reports a detailed study of the applicability of decelerating relativistic jet models to the well-resolved kiloparsec-scale structures in the nearby FR I radio galaxy 3C 31. Our intention is to deconvolve the emission mechanism (synchrotron radiation from a magnetized relativistic flow) from the radio data, without embodying specific preconceptions about the poorly known internal physics. We construct sophisticated three-dimensional models of the effects of relativistic aberration on the appearance of intrinsically symmetric magnetized jets and we fit these models to the observed total and polarized intensity distributions in 3C 31. The aim is to derive robust estimates of the velocity field, the emissivity (combining relativistic particle density and magnetic field strength) and the three-dimensional ordering of the magnetic field (purely geometrical factors independent of its strength). We regard this as a necessary first step: realistic physical models capable of being compared with observations are not yet available. We are able to reproduce many of the observed features of the jets and we conclude that our models now provide a way to obtain key constraints on the intrinsic properties of extragalactic radio jets.

Section 2 describes new VLA imaging of the jets in 3C 31 that provides a high-quality data set suitable for detailed fitting by our models. Section 3 first reviews the principles underlying the relativistic jet models, and then goes on to describe how we adjust their parameters to fit the radio intensity and polarization data. Section 4 critically discusses the model fits and reviews the main features of the inferred jet velocity field, magnetic structure and emissivity distribution. Section 5 discusses more general implications, including: specific problems associated with reproducing the properties of the jets in the region closest to the galactic nucleus; the reasons for the sudden onset of deceleration; evidence for interaction between the jet and the surrounding medium and the applicability of adiabatic models.

Section 6 illustrates how the jets in 3C 31 should appear if orientated at other angles to the line of sight and outlines the applicability of the model to other FR I sources, including those orientated at a small angle to the line of sight. Section 7 summarizes our conclusions regarding the kinematics, emissivity and field structure of the three distinct regions of the jet and their implications for future work.

Throughout this paper, we adopt a Hubble constant $H_0 = 70\,\mathrm{km\ s^{-1}\,Mpc^{-1}}$.

2 OBSERVATIONS AND IMAGES

2.1 Choice of source: the assumption of intrinsic symmetry

Our key assumption is that the bases of the two jets are intrinsically identical, antiparallel, axisymmetric stationary flows, and that the apparent differences between them result entirely from relativistic aberration.

This is an approximation in two important respects: we ignore small-scale structure in the jets, and we assume that any intrinsic or environmental asymmetries (clearly dominant on the largest scales in many objects) are small compared with relativistic effects close to the nucleus. For any individual source, it is difficult to be sure that this is the case, particularly if the asymmetry persists on all scales. There are also a few sources (e.g. 0755+379; Bondi et al. 2000) in which the counter-jet appears much wider than the main jet, an effect which cannot be produced by relativistic beaming. We argue that these cases are rare (Laing et al. 1999) and easy to recognize. If the jet/counter-jet ratio decreases with distance from the nucleus, approaching unity on large scales, then relativistic effects probably dominate, as most plausible intrinsic or environmental mechanisms would generate asymmetries which stay roughly constant or even increase with distance. A statistical study of a complete sample of FR I sources with jets selected from the B2 sample (Laing et al. 1999) suggests that the median asymptotic jet/counter-jet ratio on large scales $\approx$1.1 for the weaker sources, so the assumption of intrinsic symmetry for the jets is generally reasonable. We ensure that this assumption is self-consistent by choosing an object whose jets are straight, with similar outer isophotes on both sides of the nucleus.

We also require that the jets are bright, allowing imaging with high signal-to-noise ratio in total intensity and linear polarization, and that any effects of Faraday rotation can be accurately corrected. This led us to the choice of 3C 31 as the first source to model.

2.2 3C 31

3C 31 is an FR I radio galaxy that has long been known (e.g. Burch 1977) to have a resolved bright jet and counter-jet with a strong initial brightness asymmetry, also present on parsec scales (Lara et al. 1997), a high degree of linear polarization at centimetre wavelengths (Fomalont et al. 1980) and a significant depolarization asymmetry (Burch 1979;

Strom et al. 1983). It is identified with the dusty elliptical galaxy NGC 383 (Martel et al. 1999) that is the brightest member of a rich group of galaxies (Arp 1966; Zwicky & Kowal 1968) with an extensive hot intra-group medium (Komossa & Böhringer 1999).

We adopt a redshift of 0.0169 for the galaxy (the mean of values from Smith et al. 2000, Huchra, Vogeley & Geller 1999 and De Vaucouleurs et al. 1991), so the projected linear scale of the images is 0.34 kpc/arcsec.

2.3 VLA observations and data reduction

The observations (Table 1) were made using all four configurations of the VLA at centre frequencies of 8.46 or 8.44 GHz and a bandwidth of 100 MHz (the slight difference in frequencies between configurations has no measurable effect). They were reduced in the AIPS software package using standard self-calibration and imaging methods, with one major exception, viz. an iterative technique used to combine data from the different VLA configurations when the compact core had varied significantly between observations. In order to make the best possible images, we needed to adjust for these changes in the compact core, as well as for slight inconsistencies in the amplitude calibration of the four observing runs.

We therefore adopted the following procedure:

(i) Image and CLEAN the data from the widest (A) configuration, ensuring that the compact core is centred on a map pixel.
(ii) Self-calibrate, initially adjusting only the phases, then the amplitudes, until the best image is obtained.
(iii) Use the CLEAN components from this image as a model for phase-only self-calibration of the next widest (B) configuration.
(iv) Image both datasets *at the same resolution* in order to measure the flux density of the core.
(v) Adjust the *(u,v)* data for the larger configuration by adding or subtracting the appropriate point component to equalize the core flux densities.
(vi) Concatenate the two *(u,v)* datasets, image, CLEAN and self-calibrate phases and amplitudes as in steps (i) and (ii).
(vii) Split the datasets apart again and check that the core flux densities are consistent. If not, repeat steps (v) and (vi).
(viii) Add further VLA configurations using steps (iii) to (vii).

Two sets of images in Stokes I, Q and U were made from the combined four-configuration data set, one with full resolution (Gaussian FWHM 0.25 arcsec) and the other tapered to give a FWHM of 0.75 arcsec (Table 2). Both the Maximum Entropy and CLEAN algorithms were used to compute deconvolved I images. The compact core was subtracted from the data before Maximum Entropy deconvolution, and added in again afterwards. All images were restored with the same truncated Gaussian beam.

The result of differencing the Maximum Entropy and CLEAN I images was a high-frequency, quasi-sinusoidal ripple of near zero mean whose amplitude increased with surface brightness. This artefact clearly originated in the CLEAN image and such ripples are indeed known to be characteristic of instabilities in the CLEAN algorithm (Cornwell 1983). There was no evidence for any differences between the two images on larger scales. We therefore use only the Maximum-Entropy I images in what follows. The Q and U images were CLEANed. A first-order correction for Ricean bias (Wardle & Kronberg 1974) was made when deriving images of polarized intensity. Apparent magnetic field directions were derived from images of Q and U corrected for Faraday rotation using results from a six-frequency analysis of the polarimetry of this region at a resolution of 1.5 arcsec FWHM to be published elsewhere. The maximum correction is $\approx 9^\circ$ and Faraday depolarization is negligible.

The resulting images are almost noise-limited (Table 2), and the excellent *(u,v)* coverage and signal-to-noise ratio allow a good representation of jet structures on a wide range of scales.

Table 1. Journal of observations

Configuration	Frequency MHz	Date	Integration time (min)
A	8460	1996 Nov 12	606
B	8440	1994 Jun 6, 14	818
C	8440	1994 Dec 4	242
D	8440	1995 Apr 28	69

Table 2. Images and rms noise levels.

Resolution (arcsec)	rms noise level (μJy / beam area) I	Q/U
0.25	5.5	6.1
0.75	6.9	5.5

2.4 Source description and selection of regions to be modelled

The left panel in Fig. 1 shows the large scale structure of 3C 31 derived from lower-resolution observations at 1.4 GHz that will be published elsewhere. The jet and counter-jet bend on large scales and form two extensive sinuous plumes. The inner part of our full-resolution 8.4-GHz image is shown in the right panel. Both jets are well collimated and dim for the first 2.5 arcsec from the nucleus, flare and brighten between 2.5 and 8 arcsec and then recollimate, as noted from earlier VLA imaging at 5 GHz (Fomalont et al. 1980). Our assumption of intrinsic symmetry requires that we restrict our analysis to the straight regions of the jets shown in the rectangular box in the right panel of Fig. 1. Within this area, the outer isophotes in the main and counter-jets are

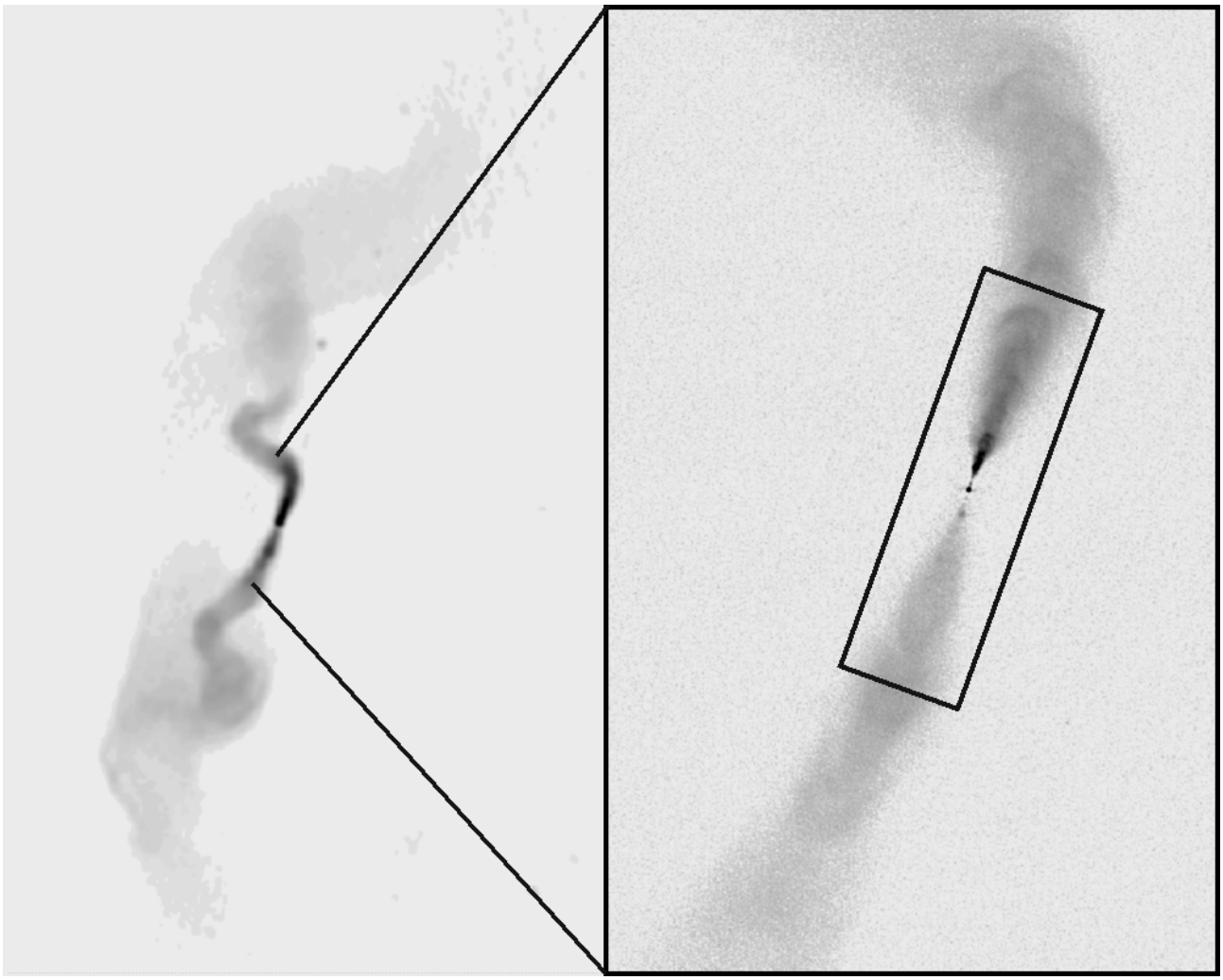

Figure 1. Montage showing the large-scale structure and jets of 3C 31. Left panel: VLA 1.4-GHz image of a 15 arcmin (300 kpc) North-South field at 5.5 arcsec (1.9 kpc) resolution. Right panel: VLA 8.4-GHz image of an approximately 2 arcmin (40 kpc) North-South field at 0.25 arcsec (85 pc) resolution. The rectangle within the right panel shows the relatively straight segment of the jets that we have chosen to model.

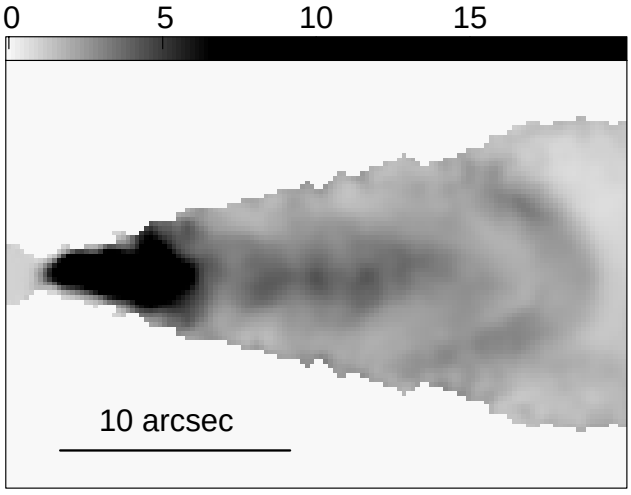

Figure 2. The observed jet/counter-jet brightness ratio (sidedness) at a resolution of 0.75 arcsec, from the 8.4-GHz observations. This was constructed by dividing the I image by a copy of itself rotated through 180° and is in the sense main jet/counter-jet.

indeed very similar. The emission from this region is well-resolved and bright enough to provide strong constraints on the velocities both along and transverse to the jet at about 1300 independent locations.

The systematic differences in brightness and polarization structure between the jets provide essential clues to the orientation and velocity field. An image of *sidedness ratio*, constructed by dividing the I image by a copy of itself rotated through 180° (in the sense main jet/counter-jet) is shown in Fig. 2. The ratio is ≈ 5 close to the nucleus and has a mean of ≈ 13 (with erratic fluctuations) from 2.5 to 6 arcsec. It drops rapidly between 6 and 8.5 arcsec, thereafter falling smoothly to ≈ 1 at the end of the modelled region. The ratio at the jet edge is almost always lower than the on-axis value, but significantly exceeds unity except at distances from the nucleus $\gtrsim 20$ arcsec.

Fig. 3 shows the degree of polarization and inferred magnetic field orientation over the inner ±27 arcsec of both jets at 0.75 arcsec resolution. The predominant pattern of the apparent magnetic field directions is to be perpendicular

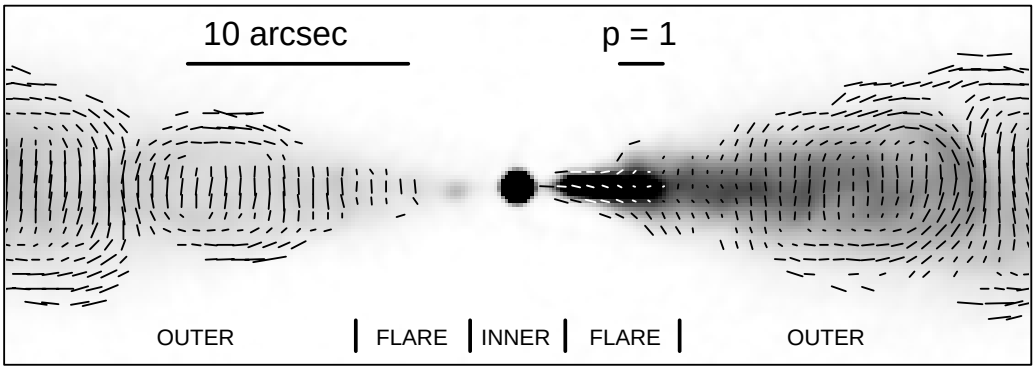

Figure 3. Vector plot showing the degree of polarization, p, and apparent magnetic field direction superposed on a total intensity grey scale at a resolution of 0.75 arcsec. The three jet regions defined in Section 3.2 are indicated by vertical bars.

to the jet axis near the centre lines of both jets, and parallel to the outer isophotes (with high degrees of polarization) at both jet edges. A notable exception to this trend occurs between 6 and 10 arcsec from the nucleus at the edges of both jets, where the degree of polarization is very small. There is a polarization asymmetry on small scales: in the bright base of the main jet, the apparent magnetic field lies along the jet axis (as is usual in FR I jets; Bridle & Perley 1984), whereas in the equivalent part of the counter-jet, it is transverse. In the outer regions, the degree of transverse-field polarization on-axis is significantly higher in the counter jet.

The jets clearly develop some internal structure (arcs and non-axisymmetric knots) before they reach the large-scale bends (Fig. 1). Similar structures are seen in linear polarization (Fig. 3): most prominently, the apparent magnetic field lies parallel to the intensity ridge lines in the arc-like structures seen on the total intensity images, producing a vortex-like appearance in the magnetic vectors. These features, which account for some tens of per cent of the brightness locally, cannot be modelled assuming that the flow is smooth, axisymmetric and stationary. Together with the large-scale bends in the jet, they effectively set the limits to which we can fit the data.

3 THE MODEL

3.1 Assumptions

Our key assumption is that the bases of the two jets are intrinsically identical, antiparallel, axisymmetric, stationary flows. We model the jets using simple parameterized expressions for the variables which determine the synchrotron emission – velocity fields, emissivity variations and intrinsic magnetic field structures – and determine the free parameters of these expressions by fitting to the observed images.

We assume that the flow is laminar and that there are no discontinuous changes of direction. If there is a turbulent velocity component (as theoretical models suggest; Section 5.2), then our technique will determine an average bulk flow speed, weighted by the distribution of Doppler beaming factors in a given region. We also assume that the variations of velocity and emissivity are continuous and smooth unless our fitting procedure explicitly requires discontinuities (this turns out to be the case at one special location: see Section 3.3).

We allow both for longitudinal deceleration as inferred from the B2 sample data (Laing et al. 1999) and for transverse velocity structure. The latter is required for two reasons. First, one class of model for relativistic jet deceleration invokes entrainment of the interstellar medium from the host galaxy across a boundary layer. A transverse velocity variation allows for the possibility that the relativistic particles near the edges of the jet move down the jet more slowly than those on the jet axis. Second, because the outer isophotes of the jets in FR I sources are usually more symmetric across the nucleus than those close to the jet axis (Laing 1993, 1996; Hardcastle et al. 1997; Laing et al. 1999), a transverse velocity variation is generally required to fit well-resolved jet brightness distributions. In order to quantify this effect, we consider two possible transverse structures. In the first (Laing 1993), a central fast *spine* with no transverse variation of velocity or emissivity is surrounded by a slower *shear layer* with gradients in both variables. In the second case, there is no distinct spine component, and the jet consists entirely of a shear layer with a truncated Gaussian transverse variation in velocity. We will refer to the two types as *spine/shear-layer (SSL)* and *Gaussian* models, respectively.

The significant linear polarization observed requires an anisotropic magnetic field. We assume that it is disordered on small scales, with negligible mean, and that the anisotropy is introduced by shear and compression. We consider large-scale ordering of the magnetic fields to be unlikely. The simplest ordered fields capable of generating the observed polarization (single helices) produce large changes in emission across the jets, which are not observed (Laing 1981; Clarke, Norman & Burns 1989). More complex ordered configurations, such as those proposed by Königl & Choudhuri (1985), cannot be as easily dismissed on observational grounds, but the presence of a significant ordered longitudinal component is ruled out by flux conservation arguments (Begelman, Blandford & Rees 1984). In any case, our conclusions on the relative magnitudes of the field components would not be seriously affected (indeed, our calculations would be unchanged if one of the three field components is vector-ordered). We quantify the anisotropy using the ratios of the rms field components along three orthogonal directions.

The spectrum of the jets between 1.4 and 8.4 GHz at a resolution of 1.5 arcsec FWHM is accurately described by a power law with a spectral index $\alpha = 0.55$ ($S_\nu \propto \nu^{-\alpha}$). The emission is therefore taken to be optically thin (we do not attempt to model the partially self-absorbed parsec-scale core). The corresponding electron energy distribution is $n(E)dE = n_0 E^{-(2\alpha+1)}dE = n_0 E^{-2.1}dE$. We assume an isotropic pitch-angle distribution relative to the field, so the degree of polarization, $p = (U^2+Q^2)^{1/2}/I$, has a maximum value of $p_0 = (3\alpha+3)/(3\alpha+5) = 0.70$.

3.2 Geometry

We define θ to be the angle between the jet axis and the line of sight. z is a coordinate along the jet axis with its origin at the nucleus, x is measured perpendicular to the axis, $r = (x^2+z^2)^{1/2}$ is the distance from the nucleus and ϕ is an angle measured from the jet axis ($x = z\tan\phi$). The first step in our procedure is to define functional forms for the outer surfaces of the jets and for the flow streamlines. The latter inevitably involves some guesswork, to be justified post hoc by the quality of the model fit. Inspection of the outer isophotes shows that the jets can be divided into three regions:

(i) *Inner (0 – 2.5 arcsec):* a cone, centred on the nucleus, with a half-opening angle of 8.5 degrees.
(ii) *Flaring (2.5 – 8.3 arcsec):* a region in which the jet initially expands much more rapidly and then recollimates.
(iii) *Outer (8.3 – 28.3 arcsec):* a second region of conical expansion, also centred on the nucleus, but with a half-opening angle of 16.75 degrees.

All dimensions given above are as observed, i.e. projected on the plane of the sky. This pattern of an initially narrow base and a rapid expansion followed by recollimation is general in FR I jets (Bridle & Perley 1984). In what follows, we use subscripts i, f and o to refer to quantities associated with the inner, flaring and outer regions. We refer to the inner and outer boundaries separating the regions by subscripts 1 and 0. The inner boundary is the *flaring point* defined by Parma et al. (1987) and Laing et al. (1999), and we also use this term.

Guided by the shape of the outer isophotes, we assume that the flow in the inner and outer regions is along straight lines passing through the nucleus. Our general approach is to devise simple analytical functions to describe the flow in these regions, and then to interpolate across the more complex geometry of the flaring region in such a way as to preserve continuity. Families of streamlines are parameterized by the streamline index s, which varies from 0 at the inner edge of a component (spine or shear layer) to 1 at the outside edge. In the inner and outer regions, the streamlines make constant angles ϕ_i and ϕ_o with the jet axis. We define ξ_i and ξ_o to be the half-opening angles of the jet in the inner and outer regions, and ζ_i, ζ_o to be the corresponding angles for the spine. s is defined in terms of these angles in Table 3.

We require continuity of the streamlines and their first derivatives with respect to z across the flaring region. The simplest functional form that satisfies these constraints and fits the outer isophote shape for $s = 1$ in the shear layer is:

$$x = a_0(s) + a_1(s)z + a_2(s)z^2 + a_3(s)z^3$$

Table 3. Definitions of streamline indices for inner and outer regions.

Model	Inner (conical)	Outer (conical)
SSL spine	$\phi_\mathrm{i} = \zeta_\mathrm{i} s$	$\phi_\mathrm{o} = \zeta_\mathrm{o} s$
SSL shear layer	$\phi_\mathrm{i} = \zeta_\mathrm{i} + (\xi_\mathrm{i} - \zeta_\mathrm{i})s$	$\phi_\mathrm{o} = \zeta_\mathrm{o} + (\xi_\mathrm{o} - \zeta_\mathrm{o})s$
Gaussian	$\phi_\mathrm{i} = \xi_\mathrm{i} s$	$\phi_\mathrm{o} = \xi_\mathrm{o} s$

For each streamline, the values of $a_0(s)$ – $a_3(s)$ are determined uniquely and in analytic form by the continuity conditions. The natural boundaries between regions are then spherical, centred on the nucleus at distances r_1 and r_0 and therefore perpendicular to the streamlines. Fig. 4 shows sketches of the assumed geometry for the SSL model (the equivalent for the Gaussian model is essential identical, but with the spine removed).

In order to describe variations along a streamline, we use a coordinate ρ, defined as:

$$\rho = r \quad \text{(inner region)}$$
$$\rho = r_1 + (r_0 - r_1)\frac{z - r_1\cos\phi_\mathrm{i}(s)}{r_0\cos\phi_\mathrm{o}(s) - r_1\cos\phi_\mathrm{i}(s)} \quad \text{(flaring region)}$$
$$\rho = r \quad \text{(outer region)}$$

ρ is monotonic along any streamline and varies smoothly from r_1 to r_0 through the flaring region ($\rho = r = z$ on the axis). This allows us to match on to simple functional forms which depend only on r.

The functions defining the edge of the jet are constrained to match the observed outer isophotes and are fixed in a coordinate system projected on the sky. Their values in the jet coordinate system then depend only on the angle to the line of sight. The outer edge of the spine in SSL models is not constrained in this way, and the relevant parameters may be varied in order to obtain a good fit to the data.

In what follows we will refer to *streamline coordinates* defined by *longitudinal* (along a streamline), *radial* (outwards from the axis) and *toroidal* orthonormal vectors.

3.3 Parameter variations

Our approach to parameterizing the variations of velocity, emissivity and field ordering along the jets is to specify values at four standard locations: inner jet, inner boundary (just inside the flaring region), outer boundary and an arbitrary fiducial point in the outer region. There is insufficient information to constrain any variations along the inner region, so constant values are assumed there. We allow discontinuities in most variables at the inner boundary, as there is unambiguous evidence for an abrupt change in the emissivity, at least, at this position. By contrast, all quantities vary continuously through the flaring and outer regions. We

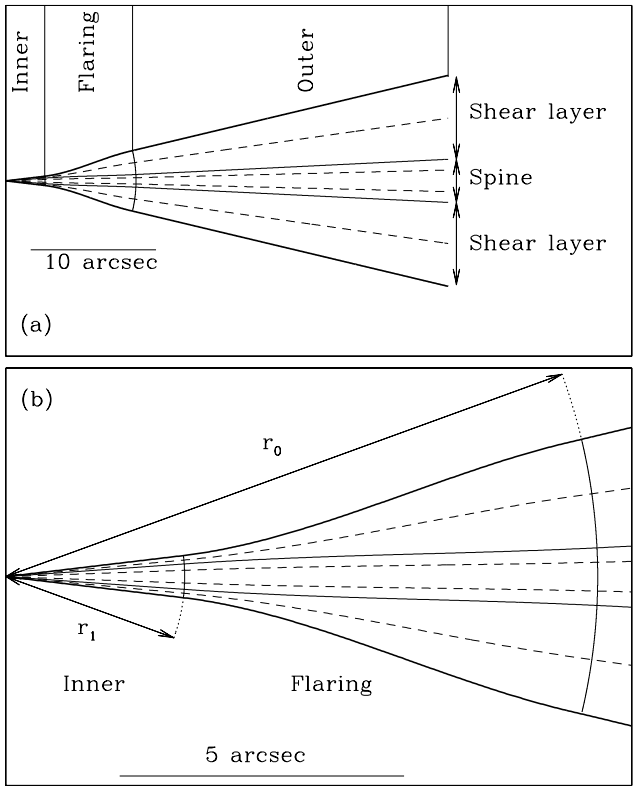

Figure 4. Geometry of the spine/shear-layer model, showing the inner, flaring and outer regions in the plane containing the jet axis. The thick full curves represent the edge of the jet, the boundaries between regions are represented by thin full curves and the $s = 0.5$ streamlines for the spine and shear layer are drawn as dashed curves. (a) The entire modelled region; (b) the base of the jet on a larger scale, showing the boundary surfaces at distances of r_1 and r_0 from the nucleus. The Gaussian model is essentially the same, but with the spine component removed.

specify their values at the three locations, together with any parameters required to specify the functional form of the variation. Table 4 summarizes the details, as follows:

Column 1: Symbol (as defined in the text),
Columns 2 – 5: the values of the quantity at the four standard locations (blank if not used),
Column 6: Any other parameters needed to quantify the variation.
Columns 7 – 9: The functional forms of the variation in the three regions.

Similarly, the functional forms used to describe transverse variations in the shear layer are listed in Table 5. There are no variations across the spine in SSL models.

3.4 Velocity field

We have chosen to model the velocity field as a separable function $\beta(\rho, s) = \beta_\rho(\rho)\beta_s(s)$ with $\beta_s(0) = 1$. The inner region is faint and poorly resolved so, in the absence of evidence to the contrary, we assume that the on-axis velocity is constant there. To generate the sideness profile of the rest of the jet (Fig. 2), the on-axis velocity must remain fairly constant throughout much of the flaring region, drop rapidly just before the outer boundary and then fall smoothly and uniformly. We chose simple functional forms for $\beta_\rho(\rho)$ to satisfy these requirements (see Table 4). The constants b_0 – b_2, c_0 and c_1 are chosen to match specified velocities at the inner and outer boundaries, and at an arbitrary fiducial point in the outer region. In addition, we require continuity of velocity and acceleration across the outer boundary so the constants are uniquely determined. These continuity conditions are not strictly necessary for the calculation described here, but are physically reasonable and essential for the adiabatic models that we discuss elsewhere.

In the flaring and outer region, $\beta_s = 1$ in the spine for SSL models, dropping linearly with s from 1 at the spine/shear layer interface to a minimum value at the edge of the jet. For Gaussian models, β_s is a truncated Gaussian function. The fact that the sidedness ratio at the edge of the jets exceeds unity over most of the modelled area (Fig. 2) means that the fractional velocity at the edge is significantly greater than zero. In both classes of model, this minimum fractional velocity, $\bar{v}(\rho)$, is allowed to vary along the jet (Table 4).

In the inner region, we found that we could not obtain satisfactory fits with linear or Gaussian transverse velocity profiles. The data required a mixture of fast and slow material, without much at intermediate velocity. Given the poor transverse resolution, we took the simple approach of assigning a single fractional velocity $\beta_s = v_\mathrm{i}$ to material in the "shear layer" (there is actually no shear). This means that the velocities of the spine and shear layer in the SSL models are decoupled, as required. For the Gaussian model, there is no separate spine component, so the inner region has a constant velocity $\beta = \beta_i$ everywhere (i.e. $\beta_s = 1$). An unphysical acceleration is required in the shear layer at the flaring point in both classes of model: this is an inevitable consequence of the increase in sidedness ratio. We discuss this problem and a possible solution in Section 5.1.

3.5 Emissivity

As with the velocity, we use a separable function for the rest-frame emissivity: $\epsilon(\rho, s) = \epsilon_\rho(\rho)\epsilon_s(s)$. We found that very different gradients of the on-axis emissivity $\epsilon_\rho(\rho)$ were required in the three regions, and therefore adopted a power-law form, with different exponents allowed for the regions, and for the spine and shear layer (Table 4). One additional parameter is needed to set the relative emissivity of spine and shear layer at a fiducial point. We enforce continuity at the outer boundary, but could not fit the data without introducing a discontinuity at the inner boundary (see Section 4.3.3). The transverse variation has the same form as that assumed for the velocity: constant in the spine, with a linear (SSL) or truncated Gaussian decrease in the shear layer to a fraction $\bar{\epsilon}(\rho)$ at the jet edge. The absolute value of the emissivity is determined by normalizing to the observed flux density.

3.6 Field ordering

Clues to the three-dimensional structure of the magnetic field come from the differences in polarization between the main and counter-jets, as summarized in Section 2.4. We initially tried the structure proposed by Laing (1993) in which

Table 4. Summary of the functional variations of velocity, emissivity and field ordering parameters along the model jets.

Quantity	Free parameters					Functional dependences		
	$0-r_1$	r_1	r_0	r_f	Other	Inner	Flaring	Outer
	Velocities							
$\beta_\rho(\rho)$	β_i	β_1	β_0	β_f	H	β_i	$b_0+b_1\rho^{H-1}+b_2\rho^H$	$c_0\exp(-c_1\rho)$
$\bar{v}(\rho)$	v_i	v_1	v_0			v_i	$v_1+\frac{(r-r_1)(v_0-v_1)}{r_0-r_1}$	v_0
	Emissivity (for each of spine and shear layer)							
$\epsilon_\rho(\rho)$					g, E_i,E_f, E_o	$g(\rho/r_1)^{-E_i}$	$(\rho/r_1)^{-E_f}$	$(r_0/r_1)^{-E_f}(\rho/r_0)^{-E_o}$
$\bar{\epsilon}(\rho)$		e_1	e_0			1	$e_1+\frac{(r-r_1)(e_0-e_1)}{r_0-r_1}$	e_0
	Field component ratios (for each of spine and shear layer)							
$j_\rho(\rho)$	j_i	j_1	j_0	j_f		j_i	$j_1+\frac{(r-r_1)(j_0-j_1)}{r_0-r_1}$	$j_0+\frac{(r-r_0)(j_f-j_0)}{r_f-r_0}$
$k_\rho(\rho)$	k_i	k_1	k_0	k_f		k_i	$k_1+\frac{(r-r_1)(k_0-k_1)}{r_0-r_1}$	$k_0+\frac{(r-r_0)(k_f-k_0)}{r_f-r_0}$

a fast, transverse-field spine with equal radial and toroidal field components is surrounded by a slower longitudinal-field shear layer. This might naively be expected from a combination of expansion and interaction with the external medium. Such a structure produces a transverse apparent field on-axis and a longitudinal field at the edge, together with a transition from longitudinal to transverse apparent field on-axis, both as observed (Fig. 3). It could be rejected for 3C 31, however, because it always requires the transition from longitudinal to transverse apparent field to occur *closer* to the nucleus in the main jet (where Doppler boosting makes the faster spine emission with its transverse apparent field relatively more prominent). The opposite is observed. The high degree of polarization observed in the outer counter-jet is also inconsistent with such a field configuration.

This suggested a model in which both the spine and the shear layer have toroidal and longitudinal field components (of roughly equal magnitude) but the radial component is everywhere very small (model B of Laing 1981). The field is then two-dimensional, in sheets wrapped around the jet axis. The apparent field is always longitudinal (with the theoretical maximum degree of polarization, p_0) at the edges of the jets, but can be either longitudinal or transverse on the axis, depending on the relative magnitudes of the two components and the angle to the line of sight. If this angle and the flow velocities are adjusted appropriately, then aberration can act so that the field sheets are seen face-on in their rest frames in the main jet (giving a low degree of polarization), but side-on in the counter-jet (leading to high polarization and a transverse apparent field). Models of this type produce much more realistic polarization distributions, especially when the ratio of toroidal to longitudinal field increases with distance from the nucleus, but still fail in two important respects. First, the field transition region in the main jet is too close to the nucleus and too short. Second, a high degree of polarization is predicted at the edge of the flaring region, where the observed values are quite low (Section 2.4). The solution to both problems is to allow a radial field component which increases from zero close to the axis to a finite value at the edge of the jet. This edge value must vary along the jet in such a way that the field is essentially isotropic at the boundary in parts of the flaring region, but the radial component vanishes at large distances from the nucleus. In contrast, we found no evidence for any transverse variation of the longitudinal/toroidal ratio in the shear layer.

Table 5. Summary of the functional variations of velocity, emissivity and field ordering parameters across the model shear layers.

Quantity	Model	Functional variation
	Velocity	
$\beta_s(s)$ $(\rho>\rho_1)$	SSL	$1+[\bar{v}(\rho)-1]s$
	Gaussian	$\exp[-s^2\ln\bar{v}(\rho)]$
$\beta_s(s)$ $(\rho<\rho_1)$	SSL	v_i
	Gaussian	1
	Emissivity	
$\epsilon_s(s)$	SSL	$1+[\bar{\epsilon}(\rho)-1]s$
	Gaussian	$\exp[-s^2\ln\bar{\epsilon}(\rho)]$
	Radial/toroidal field ratio	
$j_s(s)$		s^p

The functional forms are again given in Tables 4 and 5. We use the ratios of rms field components $j(\rho,s)$ (radial/toroidal) and $k(\rho,s)=k_\rho(\rho)$ (longitudinal/toroidal), with no transverse variation in the spine for SSL models. We chose $j(\rho,s)=j_\rho(\rho)j_s(s)$ with $j_s(s)=s^p$ for the radial/toroidal ratio. If the functional forms given for the outer region are negative, the corresponding values of j or k are set to zero.

3.7 Model integration

The principal steps in calculating the brightness distributions are as follows:

(i) Construct grids to match the observations at each of the two resolutions.

(ii) At each grid point, determine whether the line of sight passes through the jet. If so, calculate the integration limits corresponding to the outer surface of the jet and, if relevant, the spine/shear-layer interface. Separate ranges of integration are required to avoid discontinuities in the integrand.

(iii) Integrate to get the Stokes parameters I, Q and U using Romberg integration. The steps needed to determine the integrand are outlined below.

(iv) Add in the core as a point source.

(v) Convolve with a Gaussian beam to match the resolution of the observations.

(vi) Evaluate χ^2 over defined areas, using an estimate of the "noise level" derived as described later.

In order to determine the I, Q and U emissivities at a point on the line we follow an approach described in detail in Laing (2002) and based on that of Matthews & Scheuer (1990). We neglect synchrotron losses, on the grounds that the observed spectrum is a power law with $\alpha = 0.55$ between 1.4 and 8.4 GHz (and extends to much higher frequencies; Hardcastle et al. 2002). The emissivity function $\epsilon \propto n_0 B^{1+\alpha}$, where B is the total field and n_0 is the normalizing constant in the electron energy distribution as defined in Section 3.1. The observed emissivity can be calculated in the formalism developed by Laing (2002) by considering an element of fluid which was initially a cube containing isotropic field, but which has been deformed into a cuboid by stretching along the three coordinate directions by amounts proportional to the field component ratios in such a way that the value of ϵ is preserved. We calculate the synchrotron emission along the line of sight in the fluid rest frame, thus taking account of aberration.

The main steps in the calculation are:

(i) Determine coordinates in a frame fixed in the jet, in particular the radial coordinate ρ and the streamline index s, numerically if necessary.

(ii) Evaluate the velocity at that point, together with the components of unit vectors along the streamline coordinate directions (and hence the angle between the flow direction and the line of sight ψ). Derive the Doppler factor $D = [\Gamma(1 - \beta\cos\psi)]^{-1}$ and hence the rotation due to aberration ($\sin\psi' = D\sin\psi$, where ψ' is measured in the rest frame of the jet material). Rotate the unit vectors by $\psi - \psi'$ and compute their direction cosines in observed coordinates.

(iii) Evaluate the emissivity function ϵ and the rms components of the magnetic field along the streamline coordinate directions (normalized by the total field). Scale the direction cosines derived in the previous step by the corresponding field components, which are $j/(1 + j^2 + k^2)^{1/2}$ (radial), $1/(1 + j^2 + k^2)^{1/2}$ (toroidal) and $k/(1 + j^2 + k^2)^{1/2}$ (longitudinal) in the notation of the previous section.

(iv) Evaluate the position angle of polarization, and the rms field components along the major and minor axes of the probability density function of the field projected on the plane of the sky (Laing 2002). Multiply by $\epsilon(\rho, s)D^{2+\alpha}$, to scale the emissivity and account for Doppler beaming.

(v) Derive the total and polarized emissivities using the expressions given by Laing (2002) and convert to observed Stokes Q and U.

3.8 Fitting and optimization

Our basic approach is to minimize χ^2 between the model predictions and the data, summing values for the three independent Stokes parameters, I, Q and U. The value of the "noise" on the observed images is important in the optimization process, as sums of χ^2 over different areas need to be added with the appropriate weights to ensure that the data are fitted sensibly over the full range of resolutions available. The "noise" is dominated by small-scale intensity fluctuations – knots and filaments – whose amplitude is unknown a priori. Our best guess at their level comes from a measure of the deviation from axisymmetry. The "noise", Σ, is taken to be $1/\sqrt{2}$ times the rms difference between the image and a copy of itself reflected across the jet axis. This is always much larger than the off-source rms. Any contribution from deconvolution artefacts will also be included in this estimate. Some components of the small-scale structure will result in mirror-symmetric features in the brightness distribution (e.g. the bright arc in the main jet; Fig. 1), and we will therefore underestimate Σ.

We fit to the 0.25-arcsec images over the area covered by the model from 0.5 to 4.1 arcsec from the core. This excludes the core itself, and covers all of the area where significant polarized emission is detected at this resolution. Further out, the signal-to-noise ratio for these images (especially in linear polarization) is too low to provide an effective constraint, so we fit to the 0.75-arcsec images. Fits made using the high-resolution images alone are consistent with those that we describe here, but are less well constrained. χ^2 is computed only over the model area and we evaluate it at at grid-points chosen to ensure that all values are independent. There are 1346 independent points, each with measurements in 3 Stokes parameters. Of these, 44, 162 and 1140 are in the inner, flaring and outer regions, respectively.

We have optimized the models over the whole area and with one or more of the brightest small-scale features excluded from the χ^2 calculation. The derived parameters did not vary by appreciable amounts, but exclusion of the obvious "arc" in the main jet (Fig. 1) somewhat reduced the final χ^2. Given that we are effectively averaging over many small-scale filaments in the brightness distribution, we have no physical reason to remove the brightest few, but it is reassuring that the results are insensitive to their exclusion.

In order to optimize the model parameters, we use the downhill simplex method of Nelder & Mead (Press et al. 1992). This usually converges in 150 – 200 iterations given reasonable starting parameters.

3.9 Uniqueness

As with any model-fitting procedure, questions of uniqueness must be considered. Our approach is an advance on previous attempts at jet velocity estimation in several respects:

(i) We seek to fit a large quantity of well-resolved two-dimensional data, rather than one-dimensional profiles.

(ii) We have detected both jets at all distances from the nucleus, and do not have to cope with upper limits.

(iii) We fit linear polarization (Stokes Q and U) and total intensity (Stokes I) simultaneously with a small number of free model parameters. Although this introduces further

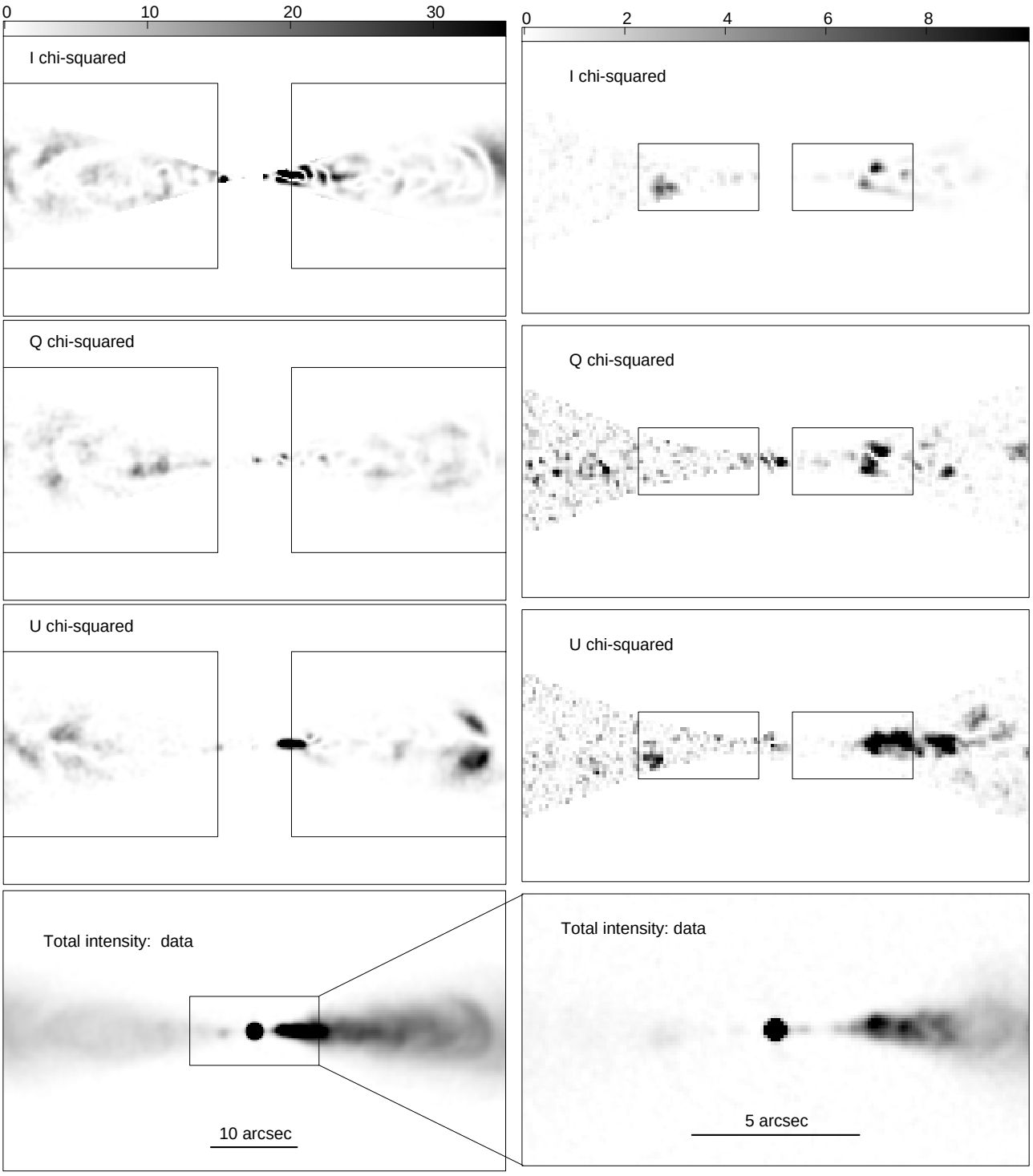

Figure 5. Grey-scale images of $\chi^2 = (S_{\rm model} - S_{\rm observed})^2/\Sigma^2$, where Σ is the "noise level" defined in the text. Left: images with a resolution of 0.75 arcsec FWHM covering an area of ± 27 arcsec from the nucleus. Right: images with 0.25 arcsec FWHM of the inner ± 7.5 arcsec. The labelled bars indicate the grey-scale ranges: these are different for the two resolutions. The boxes show the areas over which χ^2 was summed at each resolution to assess goodness of fit. From the top: χ^2 images for Stokes I, Q and U; total intensity for the same area. χ^2 values are not plotted for Stokes I in the immediate vicinity of the core.

Table 6. Summary of reduced χ^2 values.

Model type	No blanking	Arc blanked
SSL	1.71	1.51
Gaussian	1.80	1.60

degrees of freedom in order to describe the field anisotropy, we find that the form of the jet velocity field is as severely constrained by the observed polarization data as by the jet sidedness – the more traditional quantity used to infer jet velocities.

Model images that even qualitatively resemble the observations are hard to find. Although the downhill simplex algorithm is not guaranteed to converge on a global minimum in χ^2, we experimented with a wide range of initial conditions and found no other significant minima. We are therefore confident that the parameters given in the next section describe a unique solution.

4 MODEL RESULTS

4.1 Comparison between models and data

4.1.1 χ^2 values

We have optimized models with spine/shear layer and Gaussian transverse profiles. The resulting reduced χ^2 values, with and without blanking of the brightest arc in the main jet, are given in Table 6 and images of χ^2 are shown in Fig. 5. Both models fit the large-scale total intensity and polarization distributions well. Given that the "noise levels" are crudely estimated (and likely to be too low), and that the "noise" shows large-scale correlation with clearly non-Gaussian statistics, it is not unexpected that the reduced $\chi^2 \approx 1.5$–1.8 is inconsistent with a formal fit.

In what follows, we concentrate on the SSL model as the best description of velocity, emissivity and field ordering regardless of the underlying physics. The Gaussian equivalent has a smaller number of free parameters (Table 7). It gives a slightly, but significantly worse fit, except in the inner region, where it fails seriously (albeit with little effect on the overall χ^2).

4.1.2 Total intensity images and profiles

Figs 6 and 7 show the predicted and observed images of Stokes I at 0.75 and 0.25 arcsec resolution, respectively. Profiles of I along the jet axis are given at these resolutions in Figs 8 and 9. The differences between the main and counter-jets are emphasized in sidedness images and profiles (Figs 10 and 11).

4.1.3 Fitted total intensity features

The following features of 3C31 can be accurately reproduced by our chosen fitting functions after optimization:

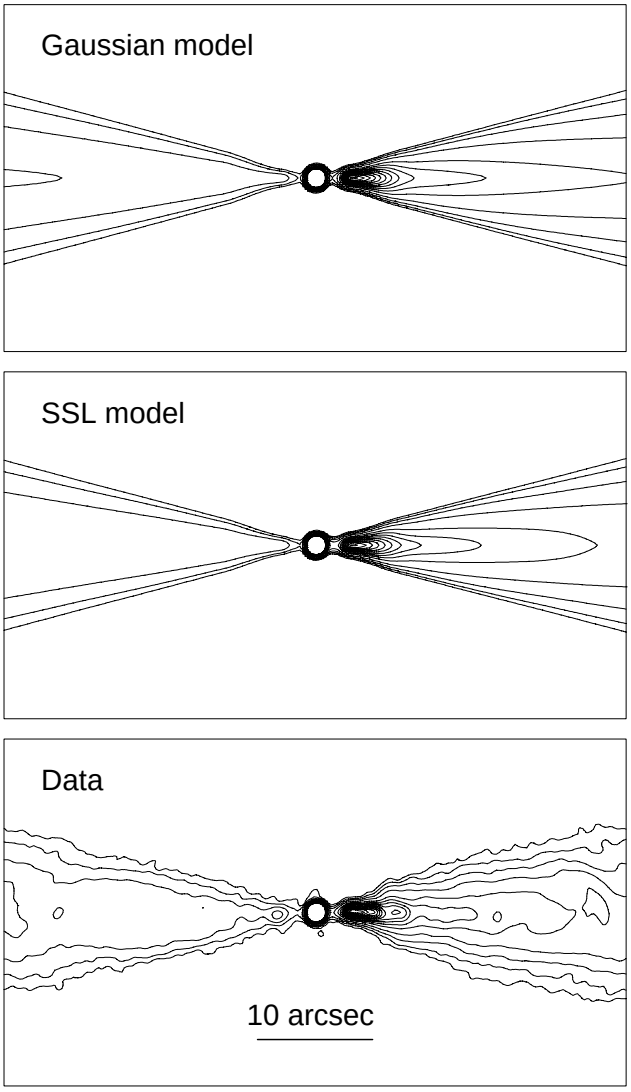

Figure 6. Contours of total intensity at a resolution of 0.75 arcsec, covering ± 27 arcsec from the nucleus. The contour levels are: -1, 1, 2, 4, 8, 16, 24, 32, 40, 48, 56, 64, 72, 80, 88, 96, $104 \times 40\,\mu$Jy/beam area. From top: model with Gaussian profile, model with spine/shear layer, VLA data.

(i) Both jets are initially faint and brighten at the beginning of the flaring region, where significant deceleration begins.

(ii) The brighter jet has a more centrally-peaked brightness distribution, while that of the counter-jet is much flatter.

(iii) The jets become more equal in brightness further from the nucleus as they decelerate (Fig. 10).

(iv) The on-axis sidedness ratio remains high ($\approx$13) over most of the flaring region, and drops abruptly at 5 arcsec from the nucleus. Thereafter, it declines slowly and monotonically but the main jet remains appreciably brighter than the counter-jet on-axis (Fig. 11).

The differences between the spine/shear layer and Gaussian models are at a low level. The former allows a lower emissivity in the spine, which leads to a flatter transverse intensity profile that agrees better with the data.

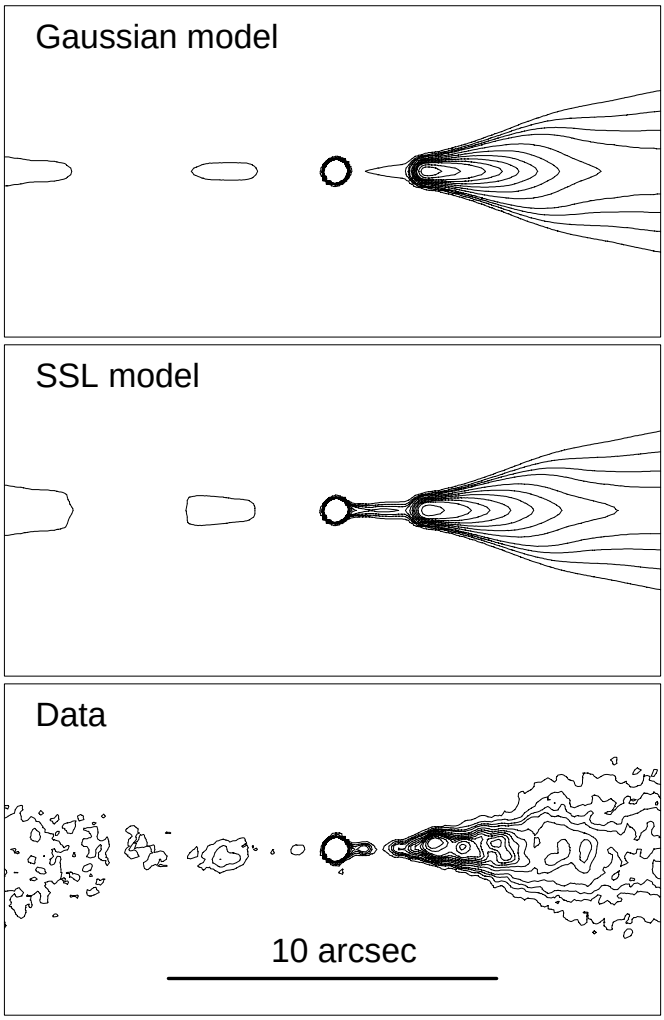

Figure 7. Contours of total intensity at a resolution of 0.25 arcsec. The plot covers ±10 arcsec from the nucleus. The contour levels are −1, 1, 2, 3, 4, 6, 8, 10, 12, 14, 16, 20, 24 × 30 μJy/beam area. From top: model with Gaussian profile, model with spine/shear layer, VLA data.

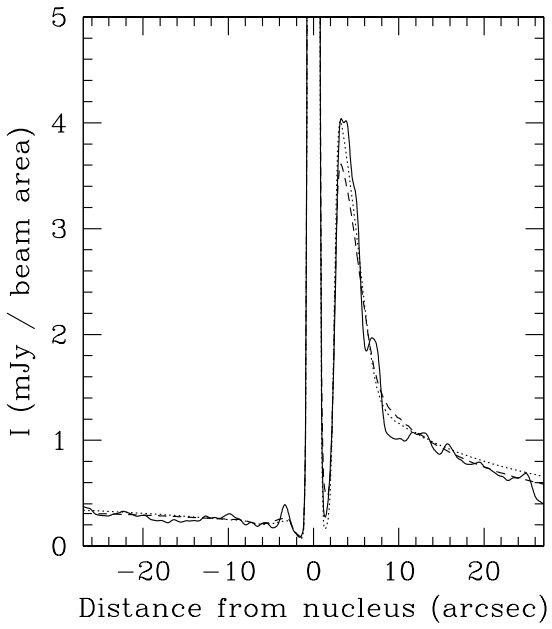

Figure 8. Total intensity profile along the jet ridge line at 0.75 arcsec resolution. Full line: data; dashed line: SSL model; dotted line: Gaussian model.

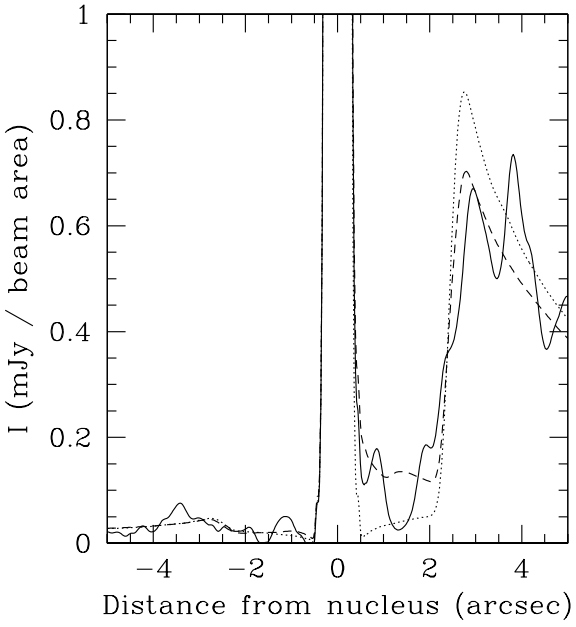

Figure 9. Total intensity profile along the jet ridge line at 0.25 arcsec resolution. Full line: data; dashed line: SSL model; dotted line: Gaussian model.

4.1.4 Polarization images and profiles

Fig. 12 shows the predicted and observed degrees of polarization $p = (Q^2 + U^2)^{1/2}/I$ at both resolutions, with the I images below them for reference. The degree and direction of polarization are represented in Figs 13 and 14 by vectors whose magnitudes are proportional to the degree of polarization and whose directions are those of the apparent *magnetic* field (i.e. rotated by 90° from the **E**-vector direction, after correcting the observations for Faraday rotation). Longitudinal and representative transverse profiles at the lower resolution are displayed in Figs 15 and 16, respectively.

4.1.5 Fitted polarization features

Our choice of fitting functions also reproduces the following features of the polarization distribution:

(i) There is a V-shaped region at the onset of the flaring of the main jet in which the polarization is close to zero on-axis and rises to values ≈40% with longitudinal apparent field at the edge (Fig. 12).

(ii) Between 4 and 8 arcsec from the nucleus in the flaring region, the main jet polarization drops to a very low level over the entire width (Fig. 12).

(iii) In contrast, the corresponding region of the counter-jet shows a transverse apparent field with monotonically in-

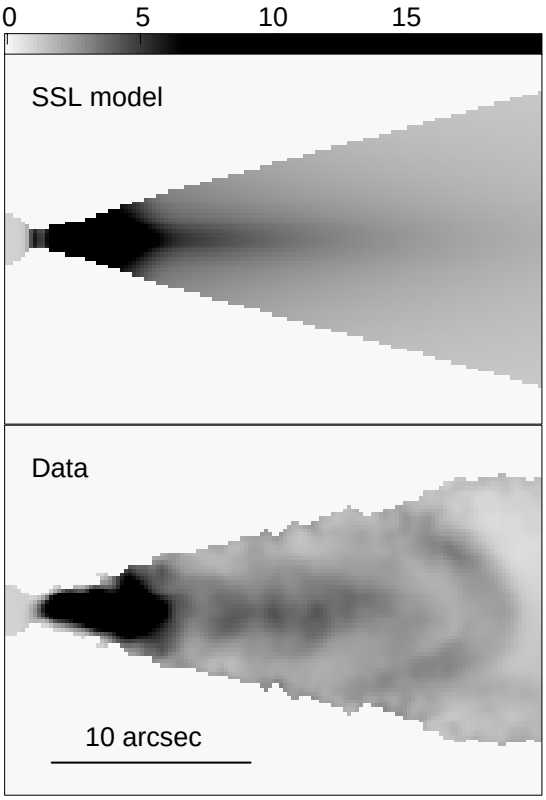

Figure 10. Grey-scale images of the observed (bottom) and SSL model (top) sidedness ratios at a resolution of 0.75 arcsec. Both images use the same transfer function, which has been optimized to emphasize the variations in sidedness in the outer part of the jet. The sidedness images for the SSL and Gaussian models are very similar, so the latter is not shown.

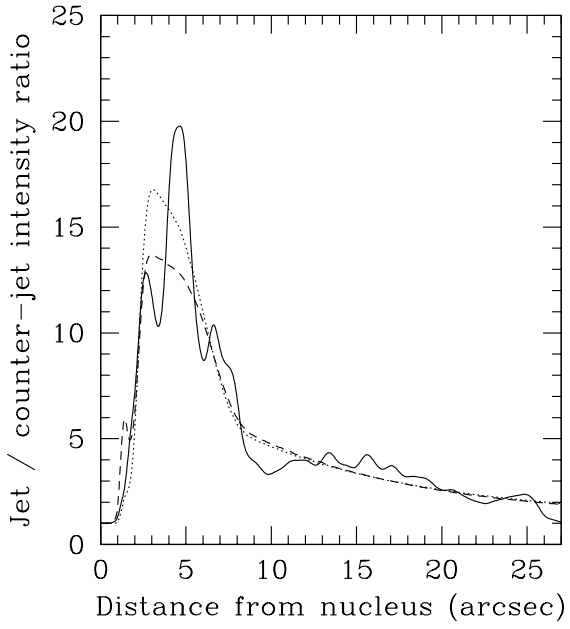

Figure 11. Profiles of jet/counter-jet sidedness ratio along the axis at a resolution of 0.75 arcsec. Full line: data; dashed: spine/shear layer model; dotted: Gaussian model.

creasing polarization on-axis with a much lower degree of polarization towards the edge (Fig. 16).

(iv) In the outer region, the degree of polarization increases monotonically with distance from the nucleus in both jets, with a transverse apparent field, but the degree of polarization is always higher in the counter-jet (Fig. 15).

(v) Both jets show longitudinal apparent field at their edges, with a degree of polarization approaching 70% at the extreme outer edge (Figs 12 and 16).

4.1.6 Features that cannot be fitted well

The models are in principle incapable of fitting non-axisymmetric or small-scale features. The most important examples of these, emphasized in the plots of χ^2 for Stokes I and U (Fig. 5) are as follows:

(i) The inner and flaring regions of the main and counter-jets have fine structure consisting of small numbers of discrete knots. These are modelled as continuous features with the correct mean level (Fig. 9).

(ii) The observed apparent magnetic field direction is oblique to the jet axis in the centre of the flaring region of the main jet (Fig. 14): this cannot be reproduced in any purely axisymmetric model.

(iii) The prominent arc of emission 20 to 24 arcsec from the nucleus in the main jet is not reproduced either in total intensity or linear polarization.

In addition, there are small but significant deviations between observed and modelled polarization patterns in the flaring region:

(i) The apparent field vectors between 5 and 7 arcsec from the nucleus in the main jet diverge more from the axis than is predicted (Fig. 14). The degree of polarization also appears to be underestimated, but the signal-to-noise ratio at 0.25 arcsec FWHM is quite low and that the observed vectors are blanked on polarized flux. There is therefore a tendency for the degree of polarization to be spuriously high for the plotted vectors. This effect has been corrected to first order (Section 2.3), but some residual remains.

(ii) The degree of polarization along the ridge-line of the counter-jet is underestimated, significantly so between 3 and 10 arcsec from the core (Figs 15 and 16).

4.2 Model parameters and confidence limits

The optimization problem is complicated, and estimates of some of the parameters are strongly correlated. In addition, we do not know the statistics (or even the rms level) of the "noise" a priori and we have imposed additional constraints by our choice of fitting functions. The χ^2 statistic is effective in optimizing the fit, but assessing confidence limits (e.g. by a Bayesian analysis or using bootstrap techniques) would be far from straightforward. We have instead adopted a simple ad hoc procedure, by which we vary a single parameter until the *fractional* increase in the χ^2 values for I or Q and U in *one* of the inner, flaring or outer regions corresponds to the formal 99% confidence limit for independent Gaussian errors and the appropriate number of degrees of freedom. Most parameters affect the fit significantly only for part of the jet, or for a subset of the Stokes parameters, so this approach

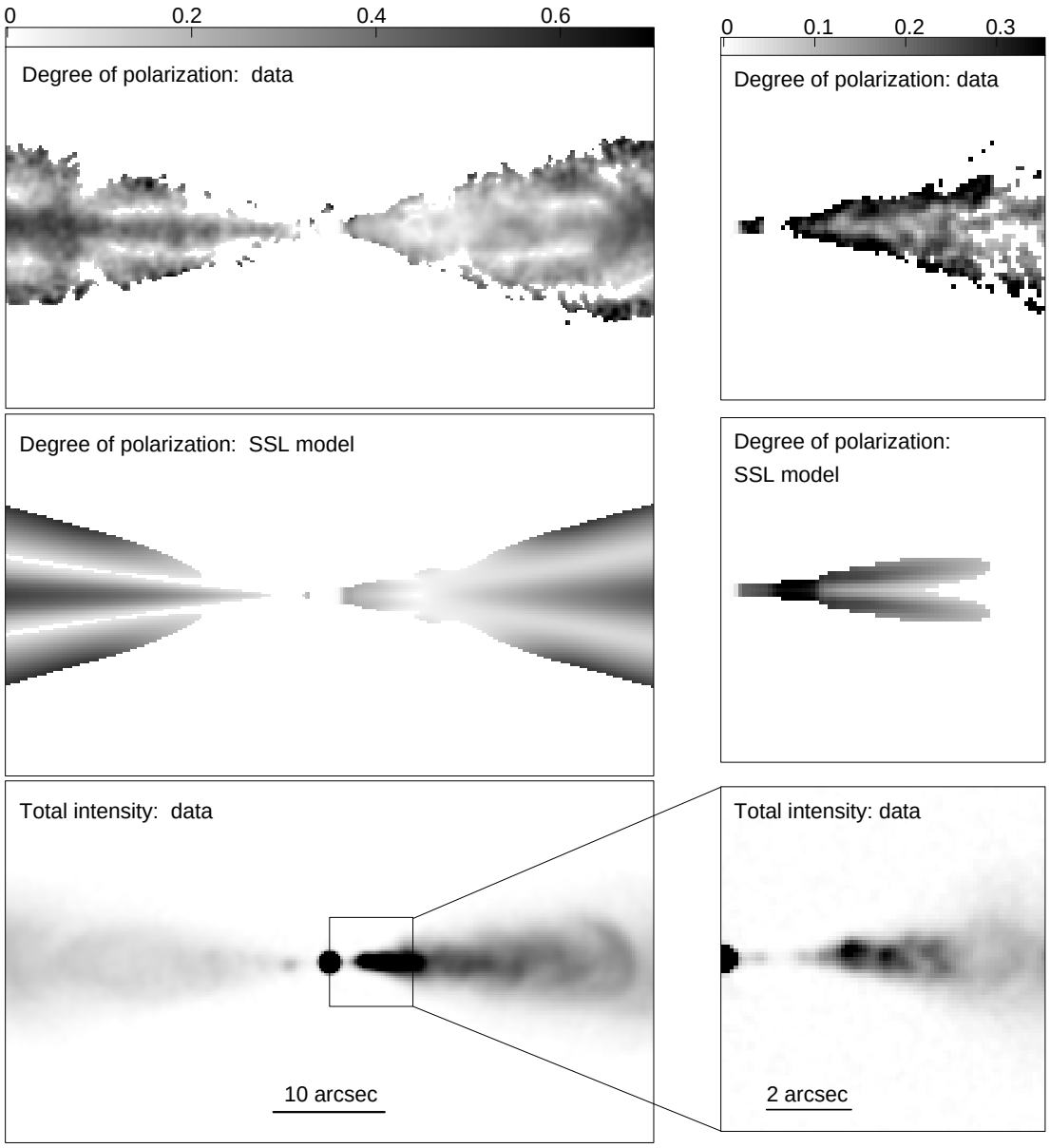

Figure 12. Grey-scale images of the total intensity and degree of polarization, p, at a resolution of 0.75 arcsec (left) and 0.25 arcsec (right). The labelled bars give the grey-scale levels for p and are different for the two resolutions. From top: polarization data, polarization of model with spine and shear layer, total intensity data. The data and models have been blanked wherever the polarized signal is $< 3\sigma$ or the total intensity is $< 5\sigma$, using the values of off-source noise, σ, given in Table 2.

is superior to one based on the total χ^2. The estimates are qualitatively reasonable, in the sense that varying a parameter by its assigned error leads to a visibly unacceptable fit, and we believe that they give a good general impression of the range of allowed models. The numerical confidence levels should not be taken too seriously, however.

Table 7 gives the fitted parameters and error estimates for the spine/shear layer and Gaussian models. The parameters are the angle to the line of sight, the spine opening angles and those defined in Tables 4 – 5. The columns are:

(i) A description of the parameter. The symbols are those used in Tables 4 – 5.

(ii) The best fit for the SSL model

(iii) The minimum value allowed by the χ^2 recipe given earlier, again for the SSL model.

(iv) The corresponding maximum value.

(v) The best fit for the Gaussian model (the allowed ranges are very similar to those for the SSL model).

In general, the parameters for the Gaussian and SSL models are very similar and always agree within the quoted errors – the contribution of the spine component to the emission (and therefore to the χ^2 value) is quite small.

Table 7. Fitted parameters and error estimates.

Quantity	opt	SSL min[a]	SSL max[b]	Gauss
Angle to line of sight θ (degrees)	52.4	48.9	54.1	51.4
Jet half-opening angles (degrees)[c]				
inner region $\xi_{\rm i}$	6.7	–	–	6.6
outer region $\xi_{\rm o}$	13.2	–	–	13.0
Boundary positions (kpc)				
inner r_1	1.1	–	–	1.1
outer r_0	3.5	–	–	3.6
arbitrary fiducial $r_{\rm f}$	9.6	–	–	9.8
Spine half opening angles (degrees)				
inner region $\zeta_{\rm i}$	4.06	3.1	6.5	–
outer region $\zeta_{\rm o}$	2.79	0.7	4.5	–
On – axis velocities / c				
inner jet $\beta_{\rm i}$	0.87	0.83	0.93	0.20
inner boundary β_1	0.77	0.68	0.83	0.76
outer boundary β_0	0.55	0.45	0.63	0.54
outer fiducial $\beta_{\rm f}$	0.28	0.25	0.33	0.27
velocity exponent H	9.5	3.6	$>$	8.8
Fractional velocity at edge of jet[d]				
inner jet $v_{\rm i}$	0.06	0.0	1.15	–
inner boundary v_1	0.74	0.4	1.30	0.97
outer boundary v_0	0.67	0.51	0.87	0.63
On – axis emissivity exponents				
inner spine $E_{\rm i}$	1.96	$<$	2.3	–
flaring spine $E_{\rm f}$	2.52	1.9	2.9	–
outer spine $E_{\rm o}$	2.14	1.4	3.8	–
inner shear layer $E_{\rm i}$	1.33	$<$	2.2	0.75
flaring shear layer $E_{\rm f}$	3.10	2.9	3.4	3.08
outer shear layer $E_{\rm o}$	1.42	1.33	1.54	1.44
Fractional emissivity at edge of jet				
inner boundary e_1	0.27	0.05	0.52	0.37
outer boundary e_0	0.20	0.09	0.28	0.26
Shear layer / spine emissivity ratio at inner boundary	2.11	1.5	3.1	–
Emissivity ratio at inner boundary (inner / flaring region)				
spine g	0.37	0.13	0.53	–
shear layer g	0.04	0.003	0.08	0.05

[a] The symbol $<$ means that any value smaller than the quoted maximum is allowed.
[b] The symbol $>$ means that any value larger than the quoted minimum is allowed.
[c] Opening angles and boundary locations are given in the jet coordinate system. The jet opening angles and the boundary locations are determined by the outer isophotes once the angle to the line of sight is specified , so no errors are quoted.
[d] The upper limits on the fractional velocity at the edge of the jet in the inner region and at the inner boundary are set not by the χ^2 constraint but rather by the condition that the velocity must be $< c$.

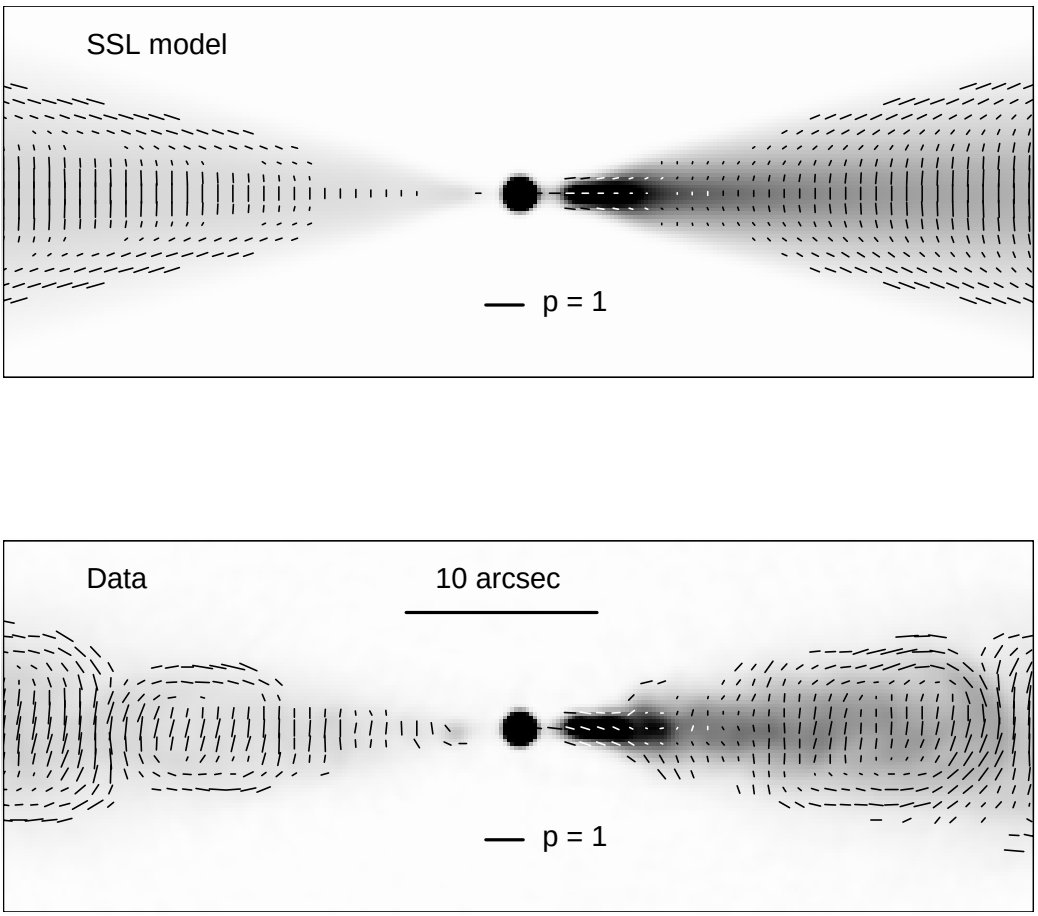

Figure 13. Vectors whose lengths are proportional to the degree of polarization, p, and whose directions are those of the apparent magnetic field superimposed on grey-scale images of total intensity at 0.75 arcsec resolution. Top: spine/shear-layer model; bottom: VLA data. The vectors are blanked as in Fig. 12.

4.3 Model description

In this sub-section, all of the plots represent a plane containing the jet axis (not projected on the sky) and distances are given in linear units.

4.3.1 Angle to the line of sight

The angle to the line of sight is one of the few parameters that affects the total and linearly-polarized emission on all scales, and is therefore particularly well constrained. The best value for both Gaussian and SSL models is $\theta \approx 52^\circ$, with uncertainties of a few degrees.

4.3.2 Velocity field

The inferred velocity field is shown as contour plots in Fig. 17 and as longitudinal profiles in Fig. 18. The on-axis velocity of the inner jet is poorly constrained, although extremely low values ($\beta < 0.4$) are ruled out. The best fits show an abrupt decrease in velocity across the inner boundary (Fig 18; see Section 5.1 for a more detailed discussion), but continuity cannot be entirely ruled out. Further out, the velocity field is much better constrained ($\pm 0.1c$ and $\pm 0.05c$, respectively, for the flaring and outer regions) and both models agree almost exactly. The on-axis velocity remains roughly constant ($\beta \approx 0.77$) between 1 and 2.5 kpc and then drops abruptly to $\beta \approx 0.55$ at the outer boundary. Quantitatively, the exponent H in the velocity law for the flaring region (Table 4) is required to be > 3. Thereafter, β declines smoothly to $\approx$0.22 at 12 kpc.

The transverse velocity profile is hardly constrained at all in the inner region. The best fits in the flaring and outer regions require an edge velocity close to 0.7 of the central value (Figs 17 and 18), independent of distance from the nucleus. The error analysis shows, however, that we cannot exclude a flat-topped profile at the inner boundary, so some evolution of the profile along the jet could occur. Very low velocities at the edge of the jet are not consistent with the observed sidedness ratios in these regions.

4.3.3 Emissivity

The spatial variation of $n_0 B^{1+\alpha}$ (proportional to the rest-frame emissivity) is shown as a grey-scale image in Fig. 19 and as longitudinal profiles in Figs 20. The emissivity is again poorly constrained in the inner region, and we can only exclude very steep decreases with distance. For the shear layer, the dependence of emissivity on distance is very

Table 7. Fitted parameters and error estimates (continued).

Quantity	SSL opt	SSL min	SSL max	Gauss
RMS field ratios (shear layer)[e]				
radial/toroidal				
inner jet centre $j_{\rm i}$	0.37	0.0	>	0.38
inner jet edge	0.0			0.0
inner boundary centre j_1	0.93	0.3	1.4	0.78
inner boundary edge $\bar{j}$	0.0			0.00
outer boundary centre j_0	1.00	0.52	1.38	0.92
outer boundary edge	0.0			0.00
fiducial distance centre $j_{\rm f}$	0.0	0.0	0.62	0.24
fiducial distance edge	0.0			0.00
index p	0.53	0.3	1.5	0.41
longitudinal/toroidal				
inner jet $k_{\rm i}$	1.23	0.2	2.3	1.43
inner boundary k_1	1.16	1.05	1.35	1.17
outer boundary k_0	0.73	0.63	0.80	0.82
fiducial distance $k_{\rm f}$	0.50	0.41	0.58	0.54
RMS field ratios (spine)				
radial/toroidal[f]				
inner jet $j_{\rm i}$	0.0	0.0	1.5	–
inner boundary j_1	0.0	0.0	1.3	–
outer boundary j_0	0.0	0.0	1.9	–
fiducial distance $j_{\rm f}$	0.0	0.0	10.0	–
longitudinal/toroidal				
inner jet $k_{\rm i}$	1.75	1.1	2.4	–
inner boundary k_1	1.06	0.7	1.8	–
outer boundary k_0	1.40	0.8	4.0	–
fiducial distance $k_{\rm f}$	0.84	0.0	8.0	–

[e] The radial/toroidal ratios always vary from 0 at the spine/shear-layer interface (SSL) or axis (Gaussian) to a maximum value at the edge of the jet (Table 5).The values quoted are for the edge and centre of the shear layer.
[f] radial/toroidal field ratios for the spine in the SSL models are consistent with 0 but poorly constrained everywhere (to the extent of having negligible influence on the χ^2 values). The relevant parameters were fixed at 0 throughout the optimization process.

different for the flaring ($\propto \rho^{-3.1}$) and outer ($\propto \rho^{-1.4}$) regions. The relative contribution from the spine is small, so its emissivity could vary either as a single power-law or in a manner closer to that of the shear layer. The fractional emissivity at the edge of the shear layer is consistent with a constant value of $\approx$0.2 in the flaring and outer regions, although a much wider range (including zero) is allowed at the inner boundary. There is strong evidence for a discontinuity in emissivity at the inner boundary for the shear layer.

4.3.4 Magnetic-field structure

Very little polarized flux is either predicted or observed to come from the inner region, and no polarized emission is detected from the inner counter-jet. For this reason, the field ratios are essentially unconstrained there (Table 7).

The toroidal field component is the largest over most of the flaring and outer regions, increasing from $\approx$0.6 to $\approx$0.9 of the total between the inner boundary and the end of the modelled region (Fig. 21). The longitudinal component, conversely, decreases from $\approx$0.7 to $\approx$0.4 over the same distance. We found no evidence for any variation of the longitudinal/toroidal field ratio across the shear layer. The component ratios for the spine are not well determined (Table 7) and could quite plausibly be identical to those for the shear layer.

Close to the edge of the jet in the flaring region, the radial component becomes appreciable, reaching a maximum of $\approx$0.6 at the edge on the outer boundary (marked by the arrows in Fig. 21). Thereafter, it decreases rapidly with distance along the jet, becoming negligible by 9.5 kpc from the nucleus in the SSL model. The radial component, unlike the other two, increases with radius (Fig. 21). As mentioned earlier, this variation is required in order to achieve even

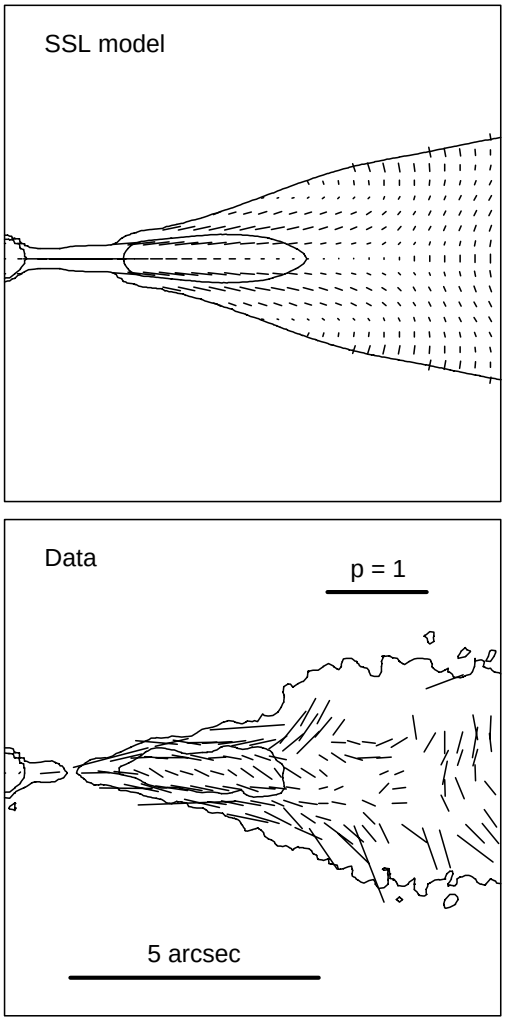

Figure 14. Vectors whose lengths are proportional to the degree of polarization, p, and whose directions are those of the apparent magnetic field superimposed on contours of total intensity at 0.25 arcsec resolution. Top: spine/shear-layer model; bottom: VLA data. The observed vectors are blanked on polarized and total intensity, as in Fig. 12, but the model vectors are plotted wherever the total intensity exceeds 5σ, regardless of polarized flux.

a qualitative fit to the observed polarization in the flaring region.

5 DISCUSSION

5.1 The inner region

Our estimates of the angle to the line of sight and the jet velocity in the inner region are entirely consistent with those of Lara et al. (1997) for the jets on parsec scales. For our preferred value of θ, their velocity range is $0.81 \leq \beta \leq 0.998$, consistent with our central velocity for the inner region ($\beta \approx 0.87$), but also allowing significant deceleration from parsec to kiloparsec scales.

The inner region poses a problem for any decelerating-jet model, in which the jet-to-counterjet intensity ratio (sidedness) must decrease with distance from the nucleus. We would expect the sidedness ratio to have a maximum in the inner region, in which case the counter-jet would be invisible. In fact, the inner region clearly has a *lower* sidedness, on average, than that in the flaring region. The brightness distribution is dominated by a few knots, so one possibility is that we are being fooled by stochastic variations. Alternatively, there could be a small amount of relatively slow-moving material in the shear layer, surrounding a fast spine.

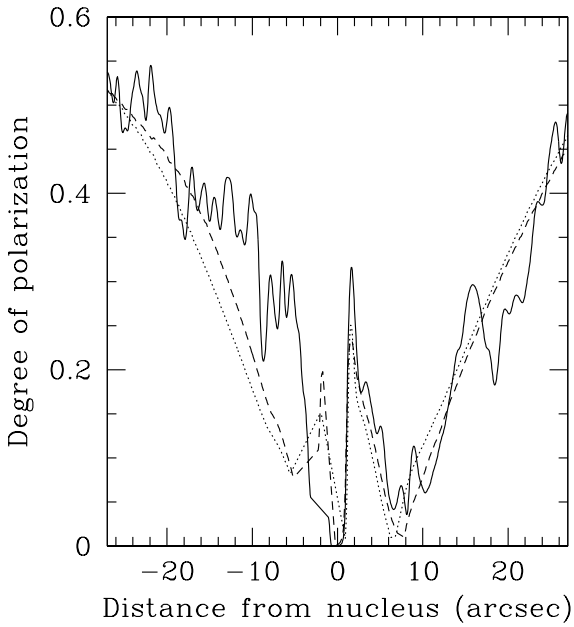

Figure 15. Profile of the degree of polarization along the jet ridge line at 0.75 arcsec resolution. Full line: data; dashed line: spine/shear layer fit; dotted line: Gaussian fit.

If a very slow component also exists further out, it cannot have a noticeable effect on the brightness distribution: the fact that the sidedness ratio at the edges of the jet in the flaring region differs significantly from unity requires that the emissivity of any very slow component becomes insignificant on large scales. This component therefore has a negligible effect on the fits beyond the inner jet, and its properties are constrained only by the intensity fits in the inner region. The faster component of the flow that dominates the outer jets is relatively faint in the inner region (because its Doppler factor and intrinsic emissivity are both lower than on larger scales), so the modelling of the inner region is almost decoupled from that of the rest of the jets in the spine/shear-layer fits.

In the best fit SSL model, the slow component has been introduced by assigning a velocity of $0.06c$ to the shear layer while the spine has a velocity of $0.87c$, i.e. we have allowed the slow component in the inner region to substitute for the faster-moving shear layer component that is required to explain the flaring region via an unphysical jump condition at the boundary. We emphasize that higher resolution imaging of the inner jets is needed to obtain firmer constraints on the transverse velocity distribution in this region, and to explore how this distribution evolves as the jet enters the flaring region. Our best guess at the geometry is sketched in Fig. 22. If this picture is correct, there must still be an increase in emissivity at the flaring point, but the values of

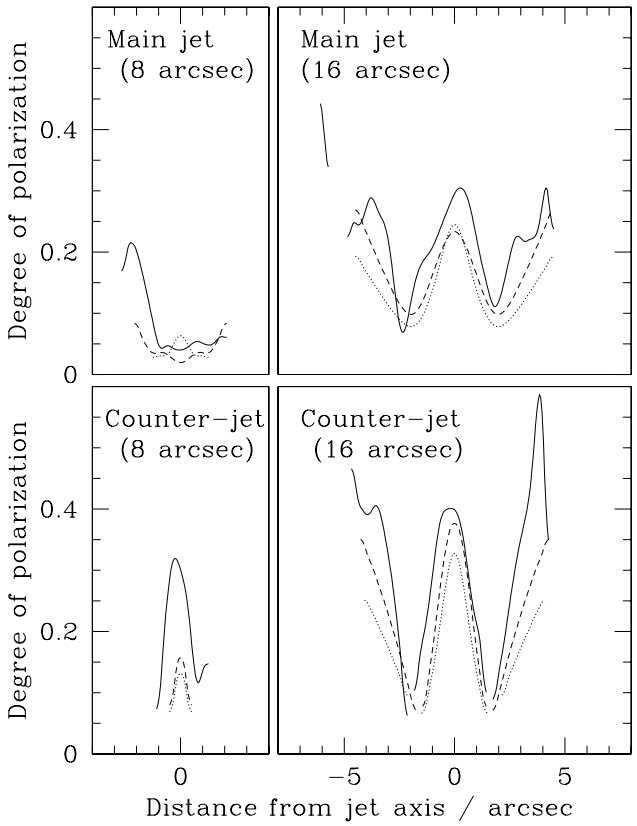

Figure 16. Example transverse profiles of the degree of polarization at distances of 8 arcsec from the core in the flaring region (left panels) and 16 arcsec from the core in the outer region (right panels). Top panels: main jet; bottom panel: counter-jet. Full line: data; dashed line: spine/shear-layer fit; dotted line: Gaussian fit. The profiles are blanked as in Fig. 12 and the resolution is 0.75 arcsec.

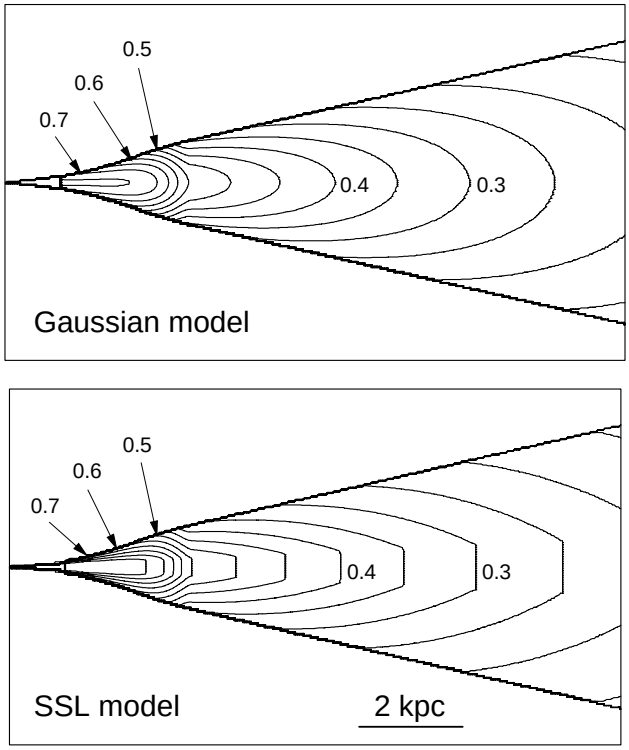

Figure 17. Contours of the velocity field for the fitted models. Top: model with Gaussian profile; bottom: model with spine and shear layer. Contours are shown at intervals of $0.05c$ and fiducial contours are labelled in the outer jets. The panels correspond to the same area projected on the plane of the sky and differ very slightly in size because the values of θ are not identical in the two models. Both cover very nearly 12 kpc in the plane of the jet.

g quoted in Table 7 will be inaccurate. Finally, we note that an additional component with β significantly higher than 0.9 would be severely Doppler-dimmed even in the approaching jet, and therefore very difficult to detect.

5.2 The onset of flaring and deceleration

We have shown that the onset of deceleration is marked by a large increase in rest-frame emissivity and a major change in the jet collimation. It is not merely that the jet becomes gradually brighter as it decelerates and Doppler suppression is reduced: there is also a discontinuity at the inner boundary.

One possibility is that the jet is supersonic, overpressured and expanding freely in the inner region. In that case, the internal pressure would fall until it drops below that of the external medium, at which point a reconfinement shock forms (Sanders 1983). The reconfinement shock is followed by a second shock at which the jet becomes *overpressured* with respect to the external medium and it this feature which is most plausibly identified with the flaring point. For a relativistic jet, Komissarov (1994) shows that the shock forms at a distance

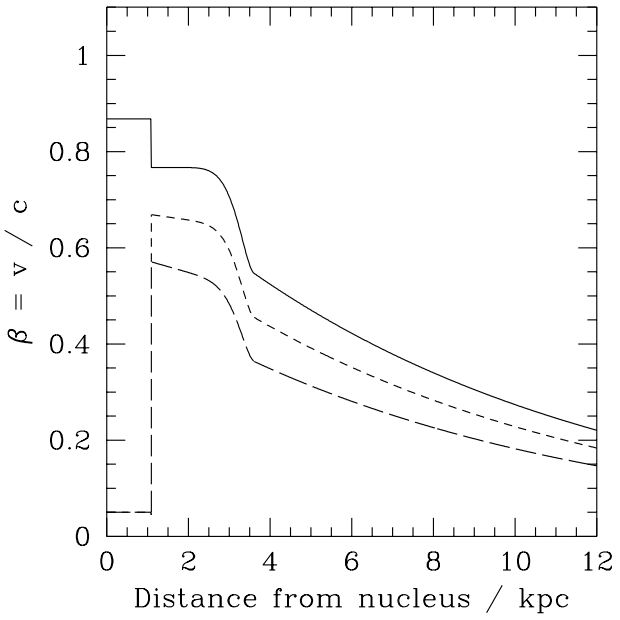

Figure 18. Profiles of the velocity along streamlines for the SSL model. Full line: spine (on-axis) and shear layer $s = 0$; short dash: shear layer $s = 0.5$; long dash: shear layer $s = 1$ (jet edge).

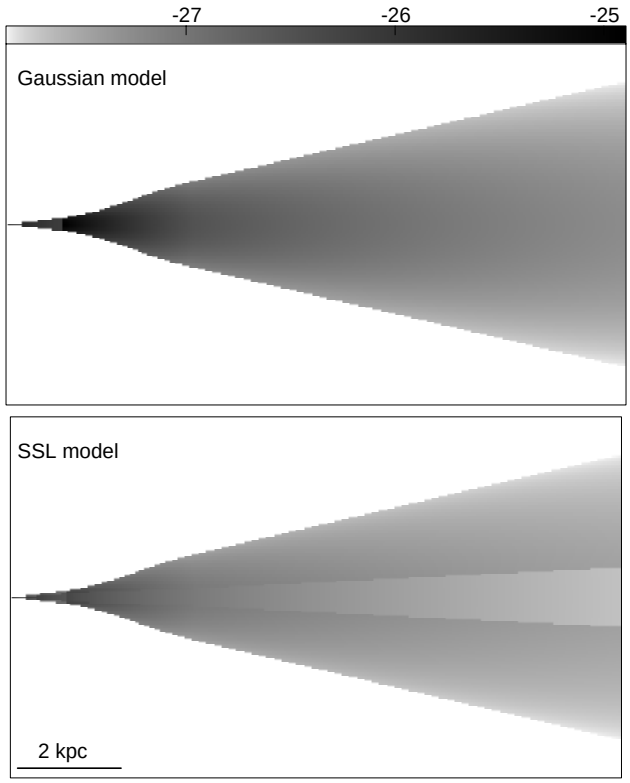

Figure 19. Grey-scale image of $\log(n_0 B^{1+\alpha})$, derived from the model emissivity, for n_0 in m^{-3} and B in T. Top: model with Gaussian profile; bottom: model with spine/shear layer. The areas covered by the two plots are not quite the same because the two models have different angles to the line of sight, but the linear scales are identical.

$$z_{\rm shock} \approx \left(\frac{2\Phi}{3\pi p_{\rm ext} c}\right)^{1/2}$$

where Φ is the energy flux through the jet and $p_{\rm ext} \approx 3\times10^{-11}$ Pa (Hardcastle et al. 2002) is the external pressure. This would be consistent with the observed inner boundary distance of 1.1 kpc for an energy flux of $\approx 5\times10^{37}$ W, somewhat higher than that the value of $\approx 1\times10^{37}$ W estimated by Laing & Bridle (2002) from a conservation-law analysis.

We see no evidence for any simple shock structure at the inner boundary, although the emission there is not completely resolved and there are obvious (non-axisymmetric) knots at the beginning of the flaring region. If the inner region is in free expansion, we can estimate the initial Mach number of the flow from the opening angle: $\arctan(\xi_{\rm i}) \approx \mathcal{M}$ where $\mathcal{M} = (\Gamma\beta)/(\Gamma_s\beta_s)$ is the generalized Mach number defined by Königl (1980), $\beta_s = c_s/c$, c_s is the internal sound speed, and $\Gamma_s = (1-\beta_s^2)^{-1/2}$. The observed value of $\xi_{\rm i} = 6.7^\circ$ corresponds to $\mathcal{M} \approx 8.5$ and hence to $\Gamma \approx 6.1$ if the inner jet has the sound speed $c_s = c/\sqrt{3}$ of an ultra-relativistic gas. This initial velocity is considerably faster than we have inferred for the inner region but, as mentioned in Section 5.1, we cannot exclude the presence of such higher-velocity material there.

A second possibility which has frequently been discussed in the literature is that the flaring point marks the onset of turbulence, or the position at which Kelvin-Helmholtz instabilities become non-linear (e.g. Baan 1980; Begelman 1982; Bicknell 1984, 1986; De Young 1996; Rosen et al. 1999; Rosen & Hardee 2000).

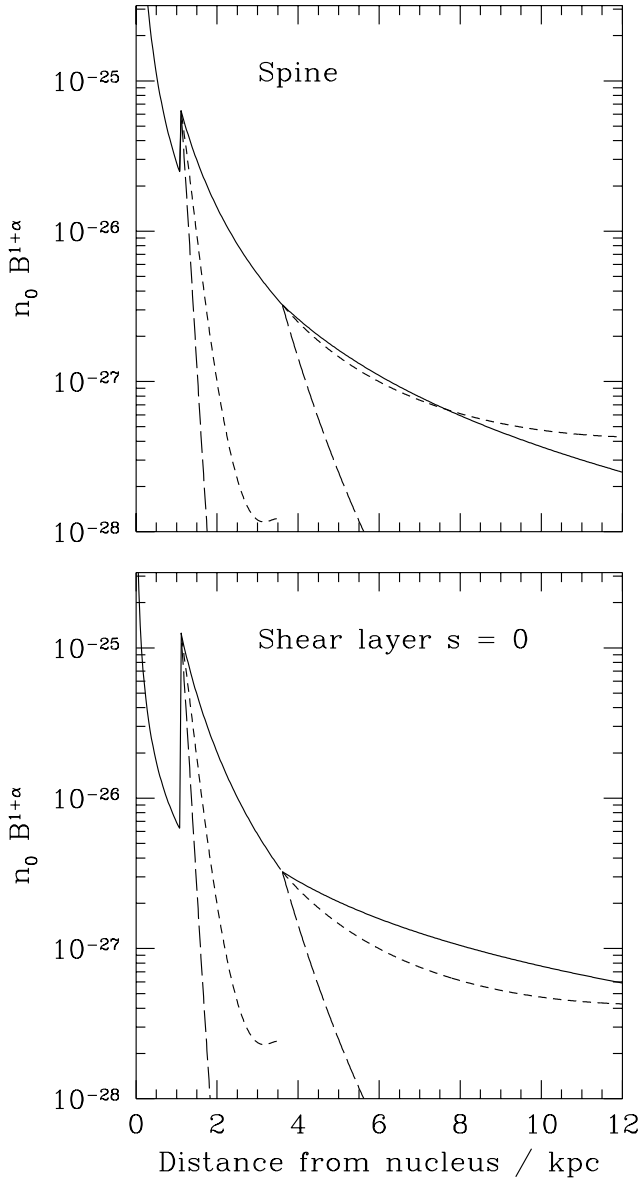

Figure 20. Profiles of $n_0 B^{1+\alpha}$ inferred from the rest-frame emissivity for two streamlines of the SSL model compared with those predicted by adiabatic models (n_0 and B are in m^{-3} and T, respectively). Full lines: SSL; long dashes: parallel-field adiabatic; short dashes: perpendicular-field adiabatic. Top panel: spine (on-axis); bottom panel: inner edge of shear layer. The adiabatic models have been arbitrarily normalized to match the SSL model profiles at the inner and outer boundaries.

We will show elsewhere (Laing & Bridle 2002) that conservation-law analysis favours the hypothesis that the flaring point is associated with a stationary shock, primarily because it suggests that the jet is over-pressured at the beginning of the flaring region. This does not, of course, exclude the subsequent development of entrainment (and presumably turbulence), as we now discuss.

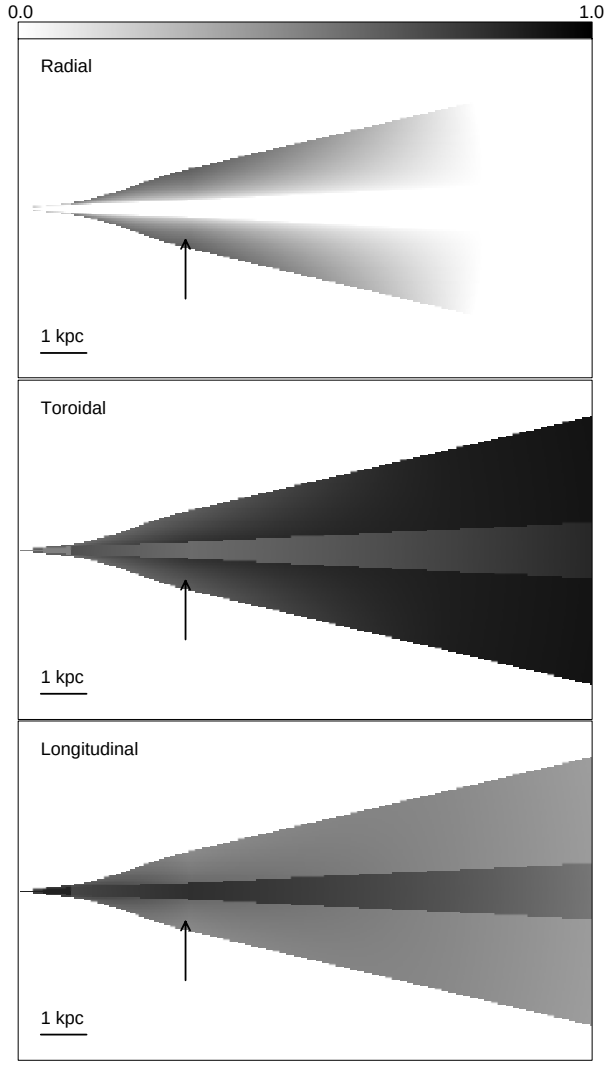

Figure 21. Grey-scale images of the rms magnitudes of the magnetic field components as fractions of the total field for the SSL model. Top: radial component $\langle B_r^2\rangle^{1/2}/B$; centre: toroidal component $\langle B_t^2\rangle^{1/2}/B$; bottom: longitudinal component $\langle B_l^2\rangle^{1/2}/B$. The arrows marks the location at the edge of the jet where the three field components are roughly equal, as discussed in the text. The radial component is constrained to be zero for the spine and the $s = 0$ streamline in the shear layer. The values for the inner region are poorly determined (Table 7).

5.3 Evidence for interaction with the surrounding medium

It is generally accepted that jets in FR I radio galaxies decelerate by picking up matter, but it is by no means clear whether the principal source of additional material is mass loss from stars (Phinney 1983; Komissarov 1994; Bowman et al. 1996) or entrainment across the jet boundary (Baan 1980; Bicknell 1984, 1986; De Young 1996): both are expected to be important. Our models require significant transverse velocity gradients, in the sense that the edge of the jet is travelling about 30% more slowly than the centre. These gradients are prima facie evidence for interaction between the flow and the external medium. There is no reason why mass input from stars should generate such gradients (Bowman et al. 1996), although a pre-existing gradient might be preserved as a jet becomes mass-loaded. The *form* of the transverse velocity profile in our best-fitting models varies surprisingly little as the jet decelerates, but the error analysis of Section 4.2 shows that the situation might be more complicated: a top-hat velocity profile at the inner boundary is consistent with the data, so the profile could still evolve significantly along the jet. The presence of large quantities of very slow material at the edges of the flaring and outer regions is firmly excluded, however (Table 7).

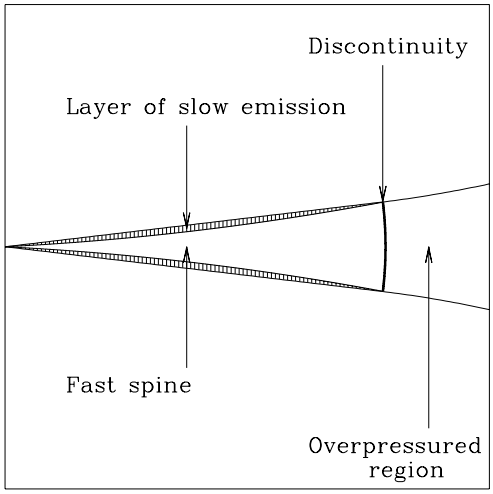

Figure 22. A sketch of one possible geometry for the inner region and its transition to the flaring region, incorporating a slow boundary layer which does not persist at large distances from the nucleus.

A second piece of evidence favouring deceleration by interaction with the external medium is the complex field structure in the flaring region, where we were forced to introduce a significant radial component, increasing towards the edge of the jet, in order to explain the low degree of linear polarization. This radial field component would not be expected from simple passive evolution of a mixture of longitudinal and toroidal field in the smooth velocity field we assume. The most natural way to generate such a radial field component is for the flow to have a disordered, turbulent character towards the jet edges such as might result from large-scale eddies. This is precisely the situation expected at the edge of the jet in the initial "ingestion" phase of the entrainment process (De Young 1996). The velocity field is then likely to have significant small-scale structure which is not included in our model, but our estimates of average bulk flow speed are unlikely to be seriously affected. Even if there is no dissipation or dynamo action in such a turbulent flow, there will be significant amplification of the magnetic field by shear, so the simplest adiabatic models, which assume laminar flow (Section 5.4), will be inappropriate.

Another way to distinguish stellar mass loading from entrainment across the jet boundary is to ask whether stellar processes can provide the mass input rate required to produce the observed deceleration. It is clear from the work of Komissarov (1994) and Bowman et al. (1996) that a jet which is decelerated purely by stellar mass loading will tend to reaccelerate on large scales, where the stellar density be-

comes low but the outward pressure gradient and buoyancy force are still appreciable. Our models require continuous deceleration in the outer region, favouring boundary-layer entrainment as the dominant mechanism there. We address this question via a conservation-law analysis in Laing & Bridle (2002), where we conclude that entrainment dominates after the beginning of the flaring region.

Little is known about the properties of turbulent relativistic shear layers, or of the viscosity mechanisms likely to predominate in magnetized relativistic jets. We cannot therefore relate the deduced velocity profiles to the internal physics of the jets. We note however that Baan (1980) computed steady-state models for viscous jets in constant-pressure atmospheres and estimated both the transverse velocity profiles and appearance of the jets (on the assumption that the emissivity is directly proportional to the viscous dissipation) for several forms of the viscosity. Baan's models generally predicted extended low-velocity wings that do not match our derived profiles. He did however discuss circumstances under which flat-topped velocity profiles such as those inferred here might arise, including that of an electron-positron jet.

5.4 The emissivity profile and adiabatic models

We have determined the variation of $n_0 B^{1+\alpha}$ (proportional to the emissivity) in the rest frame of the emitting material. Separation of this variation into particle and field contributions requires additional assumptions. The X-ray emission from the jets (Hardcastle et al. 2002) is most likely to be synchrotron, rather than inverse Compton radiation, so we cannot use it to decouple the particle and field components. We therefore postpone a discussion of the variation of pressure and density along the jet to Laing & Bridle (2002), where we also consider X-ray observations of the surrounding hot gas.

A number of authors (Baum et al. 1997; Feretti et al. 1999; Bondi et al. 2000) have recently re-opened the possibility that the jets in FR I radio galaxies are adiabatic in the sense first defined by Burch (1979), i.e. that the particles suffer only adiabatic energy losses, there are no dissipative processes causing particle acceleration or field amplification and the magnetic field is convected passively with the flow. We defer a full discussion of this question to a later paper, since our data and models are both substantially more complicated than is allowed by the analytical approaches in the literature (Baum et al. 1997). The simplest adiabatic models do not allow for any turbulent flow (Section 5.3) and there is independent evidence for particle acceleration in 3C 31's jets from X-ray observations (Hardcastle et al. 2002). Nevertheless, we can make a number of preliminary qualitative points.

We take the analytical formulae from Baum et al. (1997). In the absence of velocity shear and in the quasi-one-dimensional approximation, the field components vary as:

$$\begin{aligned} B_l &\propto x^{-2} \\ B_t &\propto (x\beta\Gamma)^{-1} \\ B_r &\propto (x\beta\Gamma)^{-1} \end{aligned}$$

where x is the jet radius. For a purely longitudinal field, this leads to a variation of the rest-frame emissivity:

$$\begin{aligned} \epsilon &\propto (\Gamma\beta)^{-(2\alpha+3)/3} x^{-(10\alpha+12)/3} \\ &= (\Gamma\beta)^{-1.37} x^{-5.83} \end{aligned}$$

and for a perpendicular field ($B_l = 0$):

$$\begin{aligned} \epsilon &\propto (\Gamma\beta)^{-(5\alpha+6)/3} x^{-(7\alpha+9)/3} \\ &= (\Gamma\beta)^{-2.92} x^{-4.28} \end{aligned}$$

The inner region poses a severe problem for the simplest adiabatic models: we have no evidence for deceleration so, if the conical region is fully filled, we would expect a very rapid brightness decline away from the nucleus ($\propto z^{-4.28}$ on-axis even in the perpendicular-field case) compared with our estimates of $\propto z^{-1.96}$ for the spine and $\propto z^{-1.33}$ for the shear layer. Even for the steepest emissivity fall-off allowed by our error analysis (Table 7), the indices are grossly discrepant. We have already argued that much of the emission in the inner region may come from a surface layer (Section 5.1) and the assumption that the radiating material expands with constant opening angle may be invalid.

For the flaring and outer regions, we have computed the emissivity variations for the parallel- and perpendicular-field cases using our model for the radius and velocity of the jet. The results are shown in Fig. 20, where we have normalized the adiabatic models to the observed emissivities at the beginnings of the flaring and outer regions. Two example streamlines are shown for the SSL model: on-axis in the spine and at the inner edge of the shear layer. The adiabatic models predict emissivities which fall far more rapidly than is observed in the flaring region: the deceleration is too little and too late to compensate for the expansion. In the outer region, by contrast, the perpendicular-field adiabatic model predicts emissivities fairly close to those observed.

There are two other fundamental problems with the adiabatic models. First, the field structure in the flaring region is not consistent with passive convection in a smooth, axisymmetric velocity field. Our assumed velocity field acts so as to shear an existing radial component, thereby amplifying the component along the flow. It cannot, therefore, create the region of approximately isotropic field at the edge of the flaring region starting with what is essentially a mixture of toroidal and longitudinal components. Second, the assumed velocity field *cannot* change the ratio of radial to toroidal field. It is clear from Fig. 21 that the radial component essentially disappears at some point after the flaring region.

We conclude that simple adiabatic models could not describe the inner and flaring regions, even if more realistic field configurations and the effects of velocity shear were to be included, but that a model of this type may apply to the outer region, at least if the radial field component is mostly eliminated by the outer boundary. Further investigation of this set of problems is outside the scope of the present paper and will be presented elsewhere.

6 3C 31 AT OTHER ANGLES TO THE LINE OF SIGHT

The best-fitting spine/shear-layer models require the jets to be at 52° to the line of sight.

Fig. 23 shows the appearance of these models if observed with the jet axis at other angles to the line of sight at a resolution of 0.75 arcsec. We have not modelled the core, but need to make a crude estimate of the dependence of its flux density on θ in order to illustrate the effects of observing with limited dynamic range. For these calculations the effective flow velocity in the core has been arbitrarily set at $\beta = 0.95$ ($\Gamma = 3.2$) and its flux is assumed to scale with angle according to the predictions of a simple single-velocity model for a pair of oppositely directed, identical jets:

$$S_c \propto [\Gamma(1-\beta\cos\theta)]^{-(2+\alpha_c)} + [\Gamma(1+\beta\cos\theta)]^{-(2+\alpha_c)}$$

The spectral index of the core, $\alpha_c = 0$. The models are shown for θ=90° (jet axes in the plane of the sky), then for θ decreasing in 20° steps to 30°. The final model is shown at θ=18° as this is close to the limiting case that our code can compute, wherein the line of sight lies inside the widest cone angle subtended by the jet outflow at the nucleus (in the flaring region).

The left panels show how the jets would appear if they could be observed at these angles to the line of sight with the same limiting sensitivity as in our VLA data for 3C 31, using logarithmically spaced contours. Fig. 24 shows a similar display for an observing resolution of 0.25 arcsec FWHM, emphasizing the changes in appearance of the inner jet and the start of the flaring region.

The θ=90° case is, of course, symmetrical with two identical centre-brightened jets that lack well-defined intensity maxima at their bases. Images of 3C 449 (Feretti et al. 1999) and PKS 1333−33 (Killeen et al. 1986) show precisely these features.

At θ=70°, we see the effects of moderate differences in the Doppler boost between the two sides: the base of the main jet appears brighter, and the counter-jet is both dimmer and less centrally-peaked than the main jet (compare 3C 296; Hardcastle et al. 1997). At θ=50°, we see essentially the symmetries observed in 3C 31's jets. Note that the counter-jet brightens on an absolute scale at lower inclination angles θ because each line of sight now intersects a longer absolute path length through both jets. At θ=30°, the bright base of the main jet is effectively contiguous with the unresolved core, and at θ=18° the characterization of the structure as a "jet" according to the usual criteria (Bridle & Perley 1984) would be questionable at this resolution. By θ=18°, the apparent flux density of the core has also increased from 0.03 Jy at θ=90° to 1.6 Jy. This makes it unlikely that the wide-angle emission from the outer layers of the jet would be detected except in observations specifically designed for high dynamic range (or low angular resolution).

The right panels illustrate this by plotting the same five models with logarithmically spaced contours at fixed percentages of the apparent peak intensity, to a limit of 1/750 of the peak. The contours are chosen to match the appearance of the left panel for the θ=90° case. These "constant dynamic range" displays probably correspond better to "standard" radio astronomical observations that have not been specially optimized to detect faint broad features in the presence of strong compact components. For θ=30° and θ=18°, most of the emission detected outside the compact core comes from close to the spine of the approaching jet. Images of BL Lac objects such as 3C 371 (Pesce et al. 2001; Wrobel & Lind 1990) and Mkn 501 (Conway & Wrobel 1995) show qualitatively similar features, although the effects of projection exaggerate deviations from axisymmetry.

Fig. 25 shows the variation of polarization with angle at two different resolutions. The relative separation of the parallel–perpendicular apparent field transitions in the main and counter-jets from the nucleus is a strong function of inclination. For the main jet, the transition point moves away from the nucleus into the flaring region as θ drops from 90 to 45°, despite the opposite effect of projection on the position of the flaring point. As θ decreases still further, the transition moves closer to the nucleus again. In contrast, the field transition in the counter-jet moves monotonically closer to the nucleus as θ decreases, with the parallel-field region being essentially invisible for $\theta \leq 30°$. The longitudinal apparent field at the edges of the jets also becomes less prominent as θ increases, and would be difficult to detect for $\theta \approx 90°$ in observations with limited sensitivity. Both effects are inevitable consequence of the toroidal/longitudinal field structure. We expect them to be general features of FR I sources, testable for complete samples even where detailed modelling is impossible because of intrinsic asymmetry or low signal-to-noise. There is little published data on field transition distances, but 3C 296 (Hardcastle et al. 1997) and 0755+379 (Bondi et al. 2000) indeed have transition points further from the nucleus in their main jets.

Figs 23–25 explicitly demonstrate the possibility of generating a variety of apparent FR I jet structures with the same physical model by varying the orientation and of unifying FR I radio galaxies with some classes of "one-sided" objects. They also illustrate the need for careful consideration of observational selection effects when analysing statistical properties of unified models. In the presence of a *range* of flow velocities both along and across every jet, observational selection through limited sensitivity and dynamic range translates into velocity selection within the jets. A key byproduct of our models may be a way to guide the statistical interpretation of jet velocities in blazar-FR I unification models, as discussed by Laing et al. (1999).

The analysis of jet sidedness and width ratios for a complete sample by Laing et al. (1999) shows that our models are likely to apply in detail to the inner parts of the majority of FR I jets (i.e. before bending and other intrinsic effects become dominant). The results of Laing et al. (1999) suggest that some model parameters vary systematically from source to source: in particular, the length of the inner region and the characteristic scale of deceleration appear to increase with radio luminosity

7 SUMMARY AND SUGGESTIONS FOR FURTHER WORK

7.1 Method

We have shown that an intrinsically symmetrical, decelerating relativistic jet model containing simple prescriptions for the velocity field and emissivity with a locally random but

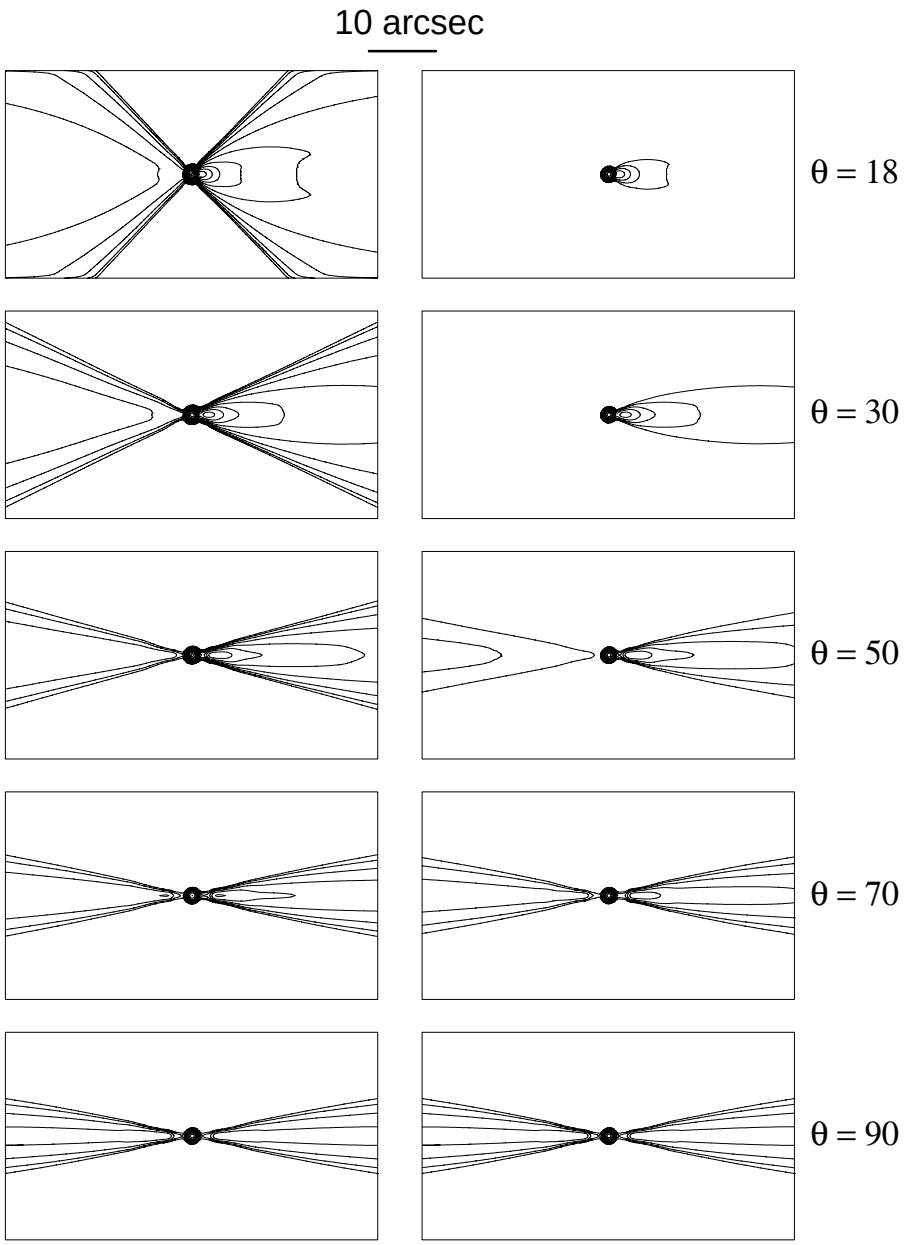

Figure 23. The best-fitting model of the 3C 31 jets viewed at various angles θ to the line of sight with a beam of 0.75 arcsec FWHM. Left panel: logarithmic contours with fixed sensitivity, i.e. with the same lowest contour in all plots. Right panel: logarithmic contours with fixed 750:1 dynamic range i.e. with the same percentages of the peak intensity in all plots. Both sets of plots cover $\pm$27 arcsec from the nucleus and the angular scale is indicated by the bar at the top of the diagram.

anisotropic magnetic field, accounts for the major features revealed by deep VLA imaging of the straight segments of the jet and counter-jet in 3C 31. The principal new features of our approach are:

(i) the use of three-dimensional (but axisymmetric) parameterized models of velocity, emissivity and field ordering;
(ii) rigorous calculation of synchrotron emission, including both relativistic aberration and anisotropy in the rest frame;
(iii) fitting to images with many independent data-points in linear polarization as well as total intensity using a robust optimization algorithm.

7.2 Principal regions of the jets

A major result of this modelling is that the three regions of the jet that were initially identified purely from the shape of the outer isophotes (Fig. 4) are also regions with distinctly different internal variations of velocity and emissivity[1].

[1] All distances in this section are measured in a plane containing the jet axis, corrected for projection using the angle to the line of sight for the best-fit SSL model.

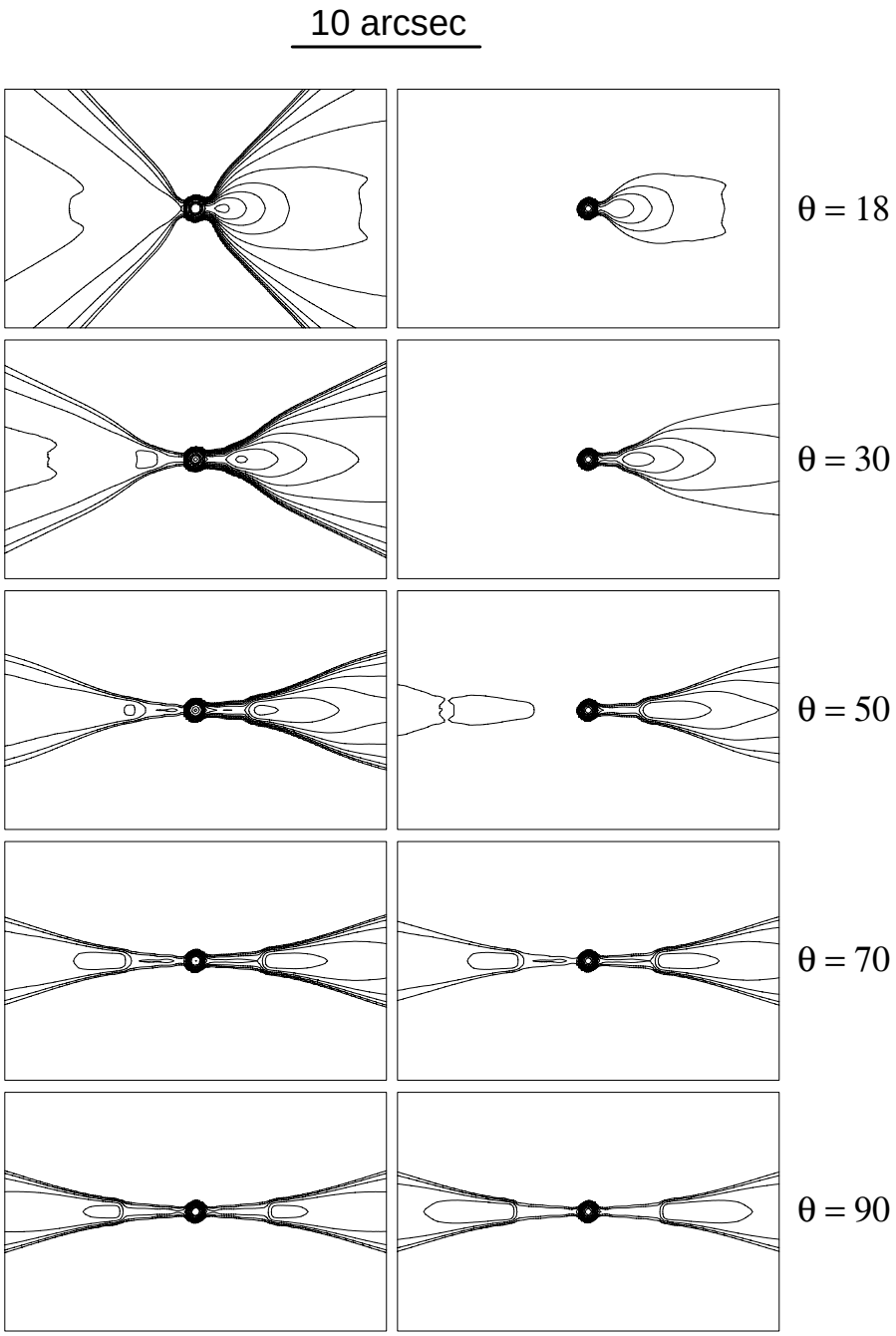

Figure 24. The best-fitting model of the 3C 31 jets viewed at various angles θ to the line of sight with a beam of 0.25 arcsec FWHM. Left panel: logarithmic contours with fixed sensitivity, i.e. with the same lowest contour in all plots. Right panel: logarithmic contours with fixed 2048:1 dynamic range i.e. with the same percentages of the peak intensity in all plots. Both sets of plots cover ± 10 arcsec from the nucleus and the angular scale is indicated by the bar at the top of the diagram.

7.2.1 The inner region (0 to 1.1 kpc)

Our conclusions for this region are tentative because of the limited transverse resolution of the data. The region is characterized by:

(i) low intrinsic emissivity;
(ii) slow lateral expansion (a cone of intrinsic half-angle 6.7°) and
(iii) a significant component of emission arising in slow-moving material.

The fitted central velocity is 0.8 – 0.9c. We have no evidence for deceleration in this region, but we cannot exclude the presence of higher-velocity (Doppler-hidden) flow components. Simple adiabatic models are grossly inconsistent with the emissivity profile.

7.2.2 Flaring region (1.1 to 3.5 kpc)

This region was defined initially by the more rapid spreading of its outer isophotes. Our modelling shows it to be a

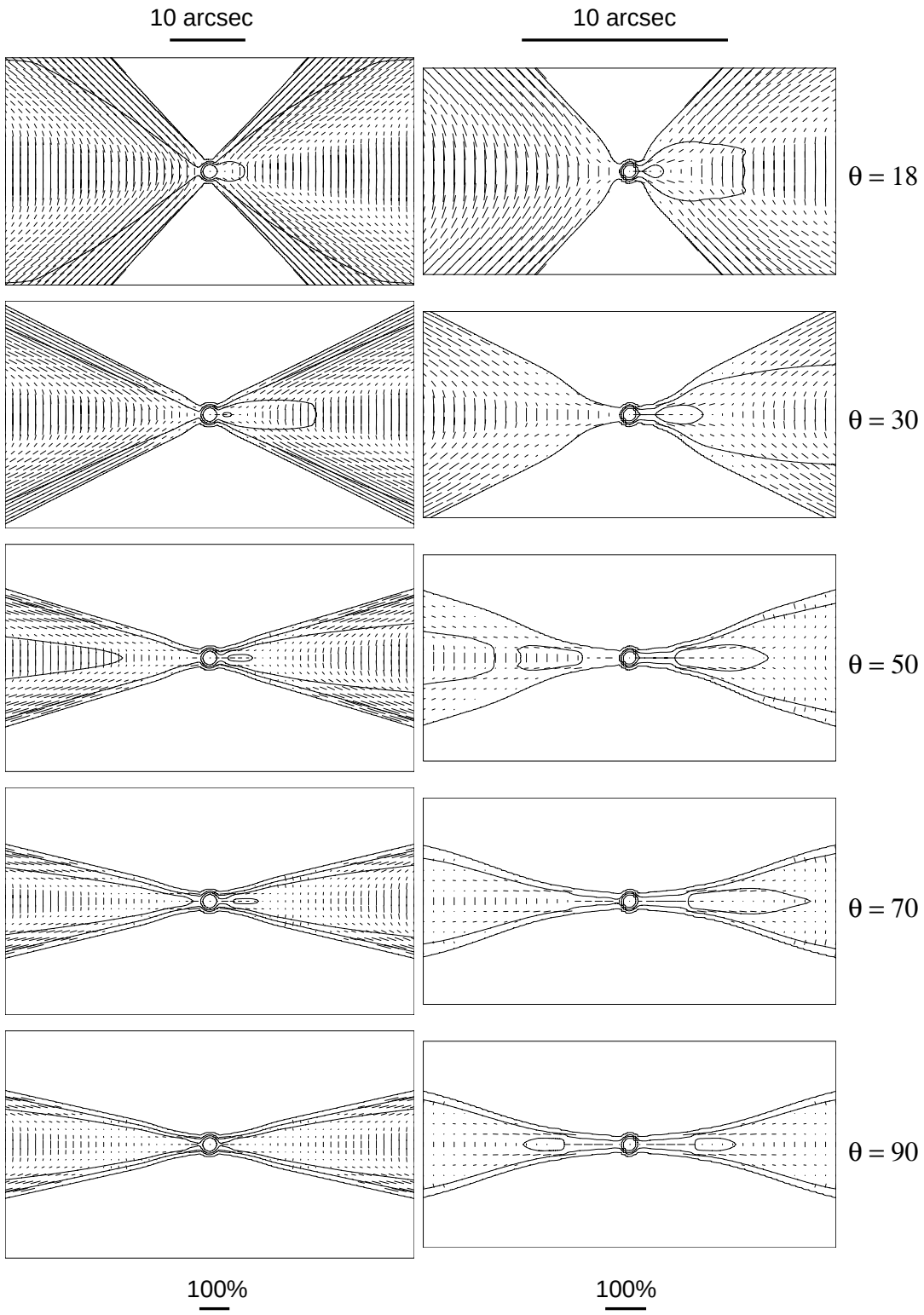

Figure 25. The best-fitting model of the 3C 31 jets viewed at various angles θ to the line of sight. Vectors whose lengths are proportional to the degree of polarization and whose directions are those of the apparent magnetic field are superimposed on selected total intensity contours. Left panels: 0.75 arcsec FWHM ($\pm$27 arcsec from the nucleus); right panels: 0.25 arcsec FWHM ($\pm$10 arcsec from the nucleus). The angular and polarization vector scales are shown at the top and bottom of the figure, respectively.

region in which several dramatic changes in the other jet characteristics occur together:

(i) The jets decelerate rapidly to an on-axis velocity of $0.55c$ after an initial slow decline from $0.77c$.
(ii) They maintain a transverse velocity profile in which the edge velocity drops to approximately 70% of the on-axis value.
(iii) The intrinsic emissivity increases abruptly at the boundary with the inner region, then declines with distance from the nucleus, z, as $z^{-3.1}$ in the shear layer and $z^{-2.5}$ in the spine.
(iv) The emissivity at the edges of the jet drops to about 20% of that on the jet axis.
(v) The radial component of the magnetic field in the shear layer becomes significant, rising from zero at the spine boundary to 90% of the toroidal and longitudinal components at the outer edge of the layer, i.e. the field is essentially isotropic at the outer boundary of the shear layer in this region.
(vi) The ratio of longitudinal to toroidal field strength decreases slightly from about 1.1 to 0.8, independent of radius in the jet.

The sudden increase in rest-frame emissivity at the flaring point suggests that there is a discontinuity in the flow, perhaps a stationary reconfinement shock system. The brightness and polarization structure in this region cannot be described by a simple adiabatic model. The transverse velocity profile and the growth of the radial field component strongly suggest that entrainment across the jet boundary becomes important.

7.2.3 Outer region (3.5 to 12 kpc)

In this region, the jets continue to expand on a cone of intrinsic half-angle 13.1°.

(i) The jets decelerate less rapidly, reaching an on-axis velocity of $0.26c$ by 10 kpc.
(ii) The intrinsic emissivity in the shear layer declines more slowly ($\propto z^{-1.4}$) with distance from the nucleus.
(iii) The transverse velocity and emissivity profiles remain essentially unchanged from those in the flaring region.
(iv) The ratio of radial to toroidal magnetic field strength decreases, becoming $< 20\%$ throughout the jet by 10 kpc.
(v) The ratio of longitudinal to toroidal magnetic field in the shear layer continues to decrease, from 0.8 to 0.5 by 10 kpc.

Although the emissivity fall-off is much closer to that predicted by a perpendicular-field, laminar adiabatic model, more work is needed to test this idea for realistic field and particle distributions.

Beyond the end of the outer region, intrinsic environmental asymmetries begin to dominate, as evidenced by the large-scale bending of both jets.

7.3 Implications for unified models

We have also calculated the change in appearance of our model brightness and polarization distributions as functions of orientation. These are in good qualitative agreement with observations of other well-observed jets and we therefore expect the model (with some parameter variations) to apply to FR I jets in general. Figures 23 and 24 show that the intensity changes are considerably more complex than would be expected for single-velocity jets. They emphasize the need for high dynamic range and sensitivity to possible wide-angle jet structures when assessing whether observed jet properties are consistent with unified models. We predict changes in polarization with orientation (Figure 25): these provide an independent test of unified models provided that our proposed field configuration is present in all FR I jets.

7.4 Further work

We now intend to model other resolvable bright jets in FR I radio galaxies to determine the extent to which their observed brightness and polarization properties resemble those of 3C 31. We expect to be able to infer their velocity, emissivity and magnetic-field distributions, building on the broad success of the jet-deceleration model in accounting for the statistical asymmetries of the B2 sample of FR I sources (Laing et al. 1999). Other sources showing well-collimated inner jets and rapid flaring include NGC 315 (Venturi et al. 1993), PKS 1333−33 (Killeen, Bicknell & Ekers 1986) and 3C 449 (Feretti et al. 1999), and it seems likely that the regimes of collimation behaviour we have identified in 3C 31 are common in FR I sources. We aim to study a sample of sources with a range of angles to the line of sight, if possible distributed isotropically, in order to test the results of Section 6. We also plan to develop a more sophisticated error analysis in order to assess confidence levels with some degree of rigour.

3C 31 has been cited as the archetypal FR I source, but is actually in the minority in having diffuse "tails" of emission extending to large distances from the core rather than confined bridges analogous to the lobes of FR II sources (De Ruiter et al. 1990). Significant differences in dynamics (especially entrainment of the surrounding medium) might be expected between the two classes. We also expect that the deceleration process should depend on the jet power and the external environment.

In Laing & Bridle (2002), we present a dynamical model for the jets in 3C 31, based on the velocity field derived in the present paper, a description of the surrounding galactic atmosphere derived from *Chandra* and ROSAT observations (Hardcastle et al. 2002) and application of conservation laws following Bicknell (1994). This approach should also be extensible to other sources. Our results favour entrainment across the boundary layer as the origin of the majority of the mass-loading of the jets in 3C 31, but it will be important to explore this in other large-scale FR I radio galaxies. We should seek further evidence for the entrainment process, such as the reduced polarization near the boundaries of the flaring regions.

Our ultimate goal is to replace the empirical descriptions of velocity, emissivity and field structure with realistic physical models. Although this is some way off, we have developed a self-consistent adiabatic model which can handle arbitrary field configurations and (laminar) velocity fields in a relativistic jet, with the aim of establishing whether any of the flow regions we have identified can be described in this way.

If our interpretation of the emission from the inner region of 3C 31's jets is correct, observations of the apparent brightness and motions of FRI jets on even smaller scales will *not* be sensitive to the properties of the underlying bulk flow, but only to those of its slowest-moving components, which may be essentially stochastic. Improved transverse resolution of the inner jets in such sources will be required to determine the origin and distribution of the slow-moving material, and the extent to which these innermost regions of FRI jets resemble the larger-scale jets in FRII sources, e.g. those in 3C 353 (Swain, Bridle & Baum 1998). This will require greater sensitivity and longer baselines than are currently available with the VLA or MERLIN.

Finally, a number of FRI sources (including 3C 31) have been detected at X-ray and/or optical wavelengths (e.g. Hardcastle, Birkinshaw & Worrall 2001; Hardcastle et al. 2002; Worrall, Birkinshaw & Hardastle 2001; Sparks et al. 2000; Kraft et al. 2002; Perlman et al. 2001; Marshall et al. 2002). The radiation is most plausibly produced by the synchrotron process over the entire observed frequency range, and the shape of the spectrum therefore carries information about particle acceleration and energy loss. It will be important to incorporate descriptions of these processes into our models.

ACKNOWLEDGMENTS

RAL would like to thank the National Radio Astronomy Observatory, the Istituto di Radioastronomia, Bologna and Alan and Mary Bridle for hospitality during this project. We thank Rick Perley for help with the observations and Matt Lister for a careful reading of the manuscript. We acknowledge travel support from NATO Grant CRG931498. The National Radio Astronomy Observatory is a facility of the National Science Foundation operated under cooperative agreement by Associated Universities, Inc.

REFERENCES

Arp, H., 1966, ApJS, 14, 1
Baan, W. A., 1980, ApJ, 239, 433
Baum, S. A., O'Dea, C. P., Giovannini, G., Biretta, J., Cotton, W. B., de Koff, S., Feretti, L., Golombek, D., Lara, L., Macchetto, F. D., Miley, G. K., Sparks, W. B., Venturi, T., Komissarov, S. S. 1997, ApJ, 483, 178 (erratum ApJ, 492, 854)
Begelman, M.C., 1982, in Heeschen, D.S., Wade, C.M., eds, IAU Symp. 97, Extragalactic Radio Sources, D. Reidel, Dordrecht, p. 223
Begelman, M.C., Blandford, R.D., Rees, M.J., 1984, Rev. Mod. Phys., 56, 255
Bicknell, G. V., 1984, ApJ, 286, 68
Bicknell, G. V., 1986, ApJ, 300, 591
Bicknell, G.V., 1994, ApJ, 422, 542
Biretta, J.A., Zhou, F., Owen, F.N., 1995, ApJ, 447, 582
Bondi, M., Parma, P., de Ruiter, H.R., Laing, R.A., Fomalont, E.B., 2000, MNRAS, 314, 11
Bowman, M., Leahy, J. P., Komissarov, S. S., 1996, MNRAS, 279, 899
Bridle, A. H., Perley, R. A., 1984, ARA&A, 22, 319
Burch, S.F., 1977, MNRAS, 181, 599
Burch, S.F., 1979, MNRAS, 187, 187
Clarke, D.A., Norman, M.L., Burns, J.O., 1989, ApJ, 342, 700
Conway, J.E., Wrobel, J.M., 1995, ApJ, 439, 98
Cornwell, T.J., 1983, A&A, 121, 281
De Ruiter, H.R., Parma, P., Fanti, C., Fanti, R., A&A, 227, 351
De Vaucouleurs, G., De Vaucouleurs, A., Corwin, H.G. Jr., Buta, R., Paturel, G., Fouque, P., Third Reference Catalogue of Bright Galaxies, Springer-Verlag, New York
De Young, D. S., 1996, in Hardee, P.E., Bridle, A.H., Zensus, J.A., eds, Energy Transport in Radio Galaxies and Quasars, ASP Conf. Series 100, 261
Fanaroff, B.L., Riley, J.M., 1974, MNRAS, 167, 31P
Feretti, L., Perley, R., Giovannini, G., Andernach, H., 1999, A&A, 341, 29
Fomalont, E. B., Bridle, A. H., Willis, A. G., Perley, R. A., 1980, ApJ, 237, 418
Hardcastle, M.J., Alexander, P., Pooley, G.G., Riley, J.M., 1997, MNRAS, 288, L1
Hardcastle, M.J., Birkinshaw, M., Worrall, D.M., 2001, MNRAS, 326, 1499
Hardcastle, M.J., Worrall, D.M., Birkinshaw, M., Laing, R.A., Bridle, A.H., 2002, MNRAS, in press
Huchra, J.P., Vogeley, M.S., Geller, M.J., 1999, ApJS, 121, 287
Killeen, N.E.B., Bicknell, G.V., Ekers, R.D., 1986, ApJ, 302, 306
Komissarov, S. S., 1994, MNRAS, 269, 394
Komossa, S., Böhringer, H., 1999, A&A, 344, 755
Königl, A., 1980, Phys. Fluids, 23, 1083
Königl, A., Choudhuri, A.R., 1985, ApJ, 289, 173 (erratum ApJ, 305, 954)
Kraft, R.P., Forman, W.R., Jones, C., Murray, S.S., Hardcastle, M.J., Worrall, D.M., 2002, ApJ, 569, 54
Laing, R.A., 1981, ApJ, 248, 87
Laing, R.A., 1988, Nature, 331, 149
Laing, R.A., 1993, in Burgarella, D., Livio, M., O'Dea, C., eds, Astrophysical Jets, Space Telescope Science Institute Symposium No.6, Cambridge University Press, Cambridge, p. 95
Laing, R.A., 1996, in Hardee, P.E., Bridle, A.H., Zensus, J.A., eds, Energy Transport in Radio Galaxies and Quasars, ASP Conf. Series 100, 241
Laing, R.A., 2002, MNRAS, 329, 417
Laing, R.A., Bridle, A.H., 2002, MNRAS, submitted
Laing, R. A., Parma, P., de Ruiter, H. R., Fanti, R., 1999, MNRAS, 306, 513
Lara, L., Cotton, W.D., Feretti, L., Giovannini, G., Venturi, T., Marcaide, J.M., 1997, ApJ, 474, 179
Martel, A., Baum, S. A., Sparks, W. B., Wyckoff, E., Biretta, J. A., Golombek, D., Macchetto, F. D., de Koff, S., McCarthy, P. J., Miley, G. K., 1999, ApJS, 122, 81
Marshall, H.L., Miller, B.P., Davis, D.S., Perlman, E.S., Wise, M., Canizares, C.R., Harris, D.E., 2002, ApJ, 564, 683
Matthews, A. P., Scheuer, P. A. G., 1990, MNRAS, 242, 616
Morganti, R., Parma, P., Capetti, A., Fanti, R., de Ruiter, H.R., 1997, A&A, 326, 919
Parma, P., de Ruiter, H.R., Fanti, C., Fanti, R., Morganti,

R., 1987, A&A, 181, 244
Perlman, E.S., Biretta, J.A., Sparks, W.B., Macchetto, F.D., Leahy, J.P., 2001, ApJ, 551, 206
Pesce, J.E., Sambruna, R.M., Tavecchio, F., Maraschi, L., Cheung, C.C., Urry, C.M., Scarpa, R., 2001, ApJ, 556, L79
Phinney, E. S., 1983, Ph.D. Thesis, University of Cambridge
Press, W.H., Teukolsky, S.A., Vetterling, W.T., Flannery, B.P., 1992, Numerical Recipes, Cambridge University Press, Cambridge.
Rosen, A., Hardee, P.E., 2000, ApJ, 542, 750
Rosen, A., Hardee, P.E., Clarke, D.A., Johnson, A., 1999, ApJ, 510, 136
Sanders, R.H., 1983, ApJ, 266, 73
Smith, R.J., Lucey, J.R., Hudson, M.J., Schlegel, D.J., Davies, R.L., 2000, MNRAS, 313, 469
Sparks, W.B., Baum, S.A., Biretta, J., Macchetto, F.D., Martel, A.R., 2000, ApJ, 542, 667
Strom, R. G., Fanti, R., Parma, P., Ekers, R. D., 1983, A&A, 122, 305
Swain, M. R., Bridle, A. H., Baum, S. A., 1998, ApJ, 507, 29
Urry, C. M., Padovani, P., 1995, PASP, 107, 803
Venturi, T., Giovannini, G., Feretti, L., Comoretto, G., Wehrle, A.E., 1993, ApJ, 408, 81
Wardle, J.F.C., Kronberg, P.P., 1974, ApJ, 194, 249
Worrall, D., Birkinshaw, M., Hardcastle, M.J., 2001, MNRAS, 326, L7
Wrobel, J. M., Lind, K. R., 1990, ApJ, 348, 135
Zwicky, F., Kowal. C. T., 1968, Catalogue of Galaxies and Clusters of Galaxies, Vol.6, California Institute of Technology